Progress in Quantum Electronics 40 (2015) 1–40

Progress in Quantum Electronics

www.elsevier.com/locate/pquantelec

Review

Hyperbolic metamaterials and their applications

Lorenzo Ferrari[a], Chihhui Wu[b,c], Dominic Lepage[d], Xiang Zhang[b,c], Zhaowei Liu[a,d,e,*]

[a]*Materials Science and Engineering, University of California, San Diego, 9500 Gilman Drive, La Jolla, CA 92093-0418, USA*

[b]*NSF Nanoscale Science and Engineering Center, University of California, Berkeley, CA 94720, USA*

[c]*Materials Sciences Division, Lawrence Berkeley National Laboratory, Berkeley, CA 94720, USA*

[d]*Department of Electrical and Computer Engineering, University of California, San Diego, 9500 Gilman Drive, La Jolla, CA 92093-0407, USA*

[e]*Center for Magnetic Recording Research, University of California, San Diego, 9500 Gilman Drive, La Jolla, CA 92093-0401, USA*

Available online 21 November 2014

Abstract

This review aims at providing a comprehensive and updated picture of the field of hyperbolic metamaterials, from the foundations to the most recent progresses and future perspectives. The topics discussed embrace theoretical aspects, practical realization and key challenges for applications such as imaging, spontaneous emission engineering, thermal, active and tunable hyperbolic media.

Keywords: Hyperbolic metamaterial; Anisotropy; Plasmonics

Contents

1. Introduction 2
2. Hyperbolic media 3
   2.1. Definition and properties 3
   2.2. Implementations 7

*Corresponding author at: Department of Electrical and Computer Engineering, University of California, San Diego, 9500 Gilman Drive, La Jolla, CA 92093-0407, USA.

E-mail address: zhaowei@ucsd.edu (Z. Liu).

http://dx.doi.org/10.1016/j.pquantelec.2014.10.001
0079-6727/

2.2.1. Multilayer . . . 8
2.2.2. Nanowire array . . . 11
3. Applications . . . 13
3.1. High-resolution imaging and lithography . . . 13
3.1.1. Hyperlens . . . 14
3.1.2. Nanolithography . . . 20
3.2. Spontaneous emission engineering . . . 22
3.3. Thermal emission engineering . . . 27
3.4. Active and tunable devices . . . 29
3.5. Emerging topics . . . 31
4. Limitations of the effective medium description and quantum size effect . . . 32
5. Conclusions . . . 34
Acknowledgments . . . 35
References . . . 36

1. Introduction

In the past decade, the development of nanofabrication techniques allowed the experimental demonstration of various kinds of optical metamaterials, designed to exhibit properties unattainable with conventional media [1]. The initial efforts were motivated by the predictions of Veselago, who in the late 1960s had envisioned a material with negative refractive index [2], a feature thus far believed to be irrealistic and – as such – of no physical relevance. His studies led eventually to artificial media exhibiting negative refraction [3], and to a critical reexamination of other paradigms in electromagnetism and related fields.

Among the varieties of metamaterials proposed and fabricated since then, hyperbolic metamaterials (HMMs) have rapidly gained a central role in nanophotonics, thanks to their unprecedented ability to access and manipulate the near-field[1] of a light emitter or a light scatterer. This feature derives directly from the excitation, inside of HMMs, of coupled surface plasmons (SPs) [4–8]. A SP is a collective oscillation of electrons, confined to the surface of a metal in contact with a dielectric. If the metal and the dielectric are shaped as thin layers, their interface is flat, and the metal surface supports *propagating* surface plasmons (or "surface plasmon polaritons" (SPPs)). If instead the metal has the shape of a nanoparticle or a nanowire, the surface of the metallic domain supports *localized* surface plasmons. The excitation of these coherent electronic vibrations is accompanied by the generation of an electromagnetic field. The latter decays very fast on both the dielectric and the metallic side, and thereby interacts principally with the near-field of the interface. When sub-wavelength metallic/dielectric layers are periodically stacked, or metallic nanowires are regularly arranged with sub-wavelength separation in a dielectric matrix, the electromagnetic fields bounded to the individual plasmonic interfaces couple, giving rise to a collective response. Such response can be interpreted, in the limit of infinite number of interfaces, as originating from bulk effective media, with a unique

[1]The *near-field* is defined by distances shorter than the wavelength of light in vacuum. Within this spatial domain, the electromagnetic field manifests a behavior that may significantly deviate from the conventional one, valid at distances much larger than one wavelength (*far-field*). The reason for this discrepancy is the loss, in the far-field, of high-momentum components of the light spectrum, which will be discussed later in the text.

anisotropic dispersion, termed hyperbolic. The interaction of these metamaterials with their near-field results in applications ranging from sub-wavelength light manipulation and imaging to spontaneous and thermal emission modification.

The present compendium reviews the conceptual and experimental milestones that established and consolidated the field of hyperbolic metamaterials, together with the latest trends. We focus our analysis on devices intended to work at optical frequencies, which span the ultraviolet, visible, near- and mid-infrared range. We start in Section 2 by introducing the properties of an ideal hyperbolic medium, and the physical phenomena that they determine (Section 2.1). Two artificial structures have been shown to possess effective hyperbolic dispersion: a multilayer (ML) and a nanowire (NW) array. We provide formulas describing the respective effective parameters and discuss their validity, also evaluating suitable material combinations (Section 2.2). Section 3 examines the most promising areas of application of HMMs. These media support the propagation of high wavevectors, a characteristic which can be exploited to break the diffraction limit. The ability of resolving sub-wavelength objects has been predicted and demonstrated with the invention of the hyperlens that we discuss alongside its implications for nanolithography in Section 3.1. HMMs can enhance the spontaneous emission (SE) of quantum sources by offering a fast decay channel with tunable and broadband features (Section 3.2). In an analogous fashion, hyperbolic modes in the infrared region can increase heat transfer and lead to a super-Planckian thermal emission in the near-field (Section 3.3). The possibility of implementing gain and mechanisms of dynamical tuning in HMMs is considered in Section 3.4, while Section 3.5 presents a miscellanea of emerging directions including enhanced absorption, waveguiding and optical forces. In Section 4 we highlight the limitations of classical hyperbolic medium models, and observe how a quantum treatment of the HMM constituent units necessarily results in spatial dispersion. A critical analysis of the limitations of HMMs and of future directions concludes our work.

2. Hyperbolic media

2.1. Definition and properties

The concept of a material with hyperbolic behavior originates from the optics of crystals. In such media, the constitutive relations connecting the electric displacement $\mathbf{D}$ and the magnetic induction $\mathbf{B}$ to the electric and magnetic fields $\mathbf{E}$ and $\mathbf{H}$ can be written as

$$\mathbf{D} = \varepsilon_0 \overline{\overline{\boldsymbol{\varepsilon}}} \mathbf{E} \tag{1}$$

$$\mathbf{B} = \mu_0 \overline{\overline{\boldsymbol{\mu}}} \mathbf{H}, \tag{2}$$

where ε_0 and μ_0 are, respectively, the vacuum permeability and permittivity, and $\overline{\overline{\boldsymbol{\varepsilon}}}$ and $\overline{\overline{\boldsymbol{\mu}}}$ are, respectively, the relative permeability and permittivity tensors. Throughout the present work we will consider nonmagnetic media, so that $\overline{\overline{\boldsymbol{\mu}}}$ simply reduces to the unit tensor. Upon diagonalization, $\overline{\overline{\boldsymbol{\varepsilon}}}$ assumes the form

$$\overline{\overline{\boldsymbol{\varepsilon}}} = \begin{bmatrix} \varepsilon_{xx} & 0 & 0 \\ 0 & \varepsilon_{yy} & 0 \\ 0 & 0 & \varepsilon_{zz} \end{bmatrix}, \tag{3}$$

in a Cartesian frame of reference oriented along the so-called *principal axes* of the crystal. The three diagonal components are all positive, and in general depend on the angular frequency ω;

the crystal is termed *biaxial* when $\varepsilon_{xx} \neq \varepsilon_{yy} \neq \varepsilon_{zz}$, *uniaxial* when $\varepsilon_{xx} = \varepsilon_{yy} \neq \varepsilon_{zz}$, and becomes *isotropic* when $\varepsilon_{xx} = \varepsilon_{yy} = \varepsilon_{zz}$.

To determine the dispersion relation of light in a medium described by Eq. (3), let us consider the following two Maxwell's equations in the absence of sources:

$$\nabla \times \mathbf{E} = -\frac{\partial \mathbf{B}}{\partial t} \tag{4}$$

$$\nabla \times \mathbf{H} = \frac{\partial \mathbf{D}}{\partial t}, \tag{5}$$

where $\mathbf{D}$ and $\mathbf{B}$ are as in Eqs. (1) and (2), respectively. By inserting into Eqs. (4) and (5) the plane wave expressions $\mathbf{E} = \mathbf{E}_0 e^{i(\omega t - \mathbf{k}\cdot\mathbf{r})}$ and $\mathbf{H} = \mathbf{H}_0 e^{i(\omega t - \mathbf{k}\cdot\mathbf{r})}$, where $\mathbf{k}$ is the wavevector, we obtain

$$\mathbf{k} \times \mathbf{E} = \omega \mu_0 \mathbf{H} \tag{6}$$

$$\mathbf{k} \times \mathbf{H} = -\omega \varepsilon_0 \bar{\bar{\boldsymbol{\varepsilon}}} \mathbf{E}. \tag{7}$$

Substitution of Eq. (6) into Eq. (7) yields the eigenvalue problem for the electric field $\mathbf{E}$:

$$\mathbf{k} \times (\mathbf{k} \times \mathbf{E}) + \omega^2 \mu_0 \varepsilon_0 \bar{\bar{\boldsymbol{\varepsilon}}} \mathbf{E} = 0, \tag{8}$$

which can be developed in matrix form:

$$\begin{bmatrix} k_0^2 \varepsilon_{xx} - k_y^2 - k_z^2 & k_x k_y & k_x k_z \\ k_x k_y & k_0^2 \varepsilon_{yy} - k_x^2 - k_z^2 & k_y k_z \\ k_x k_z & k_y k_z & k_0^2 \varepsilon_{zz} - k_x^2 - k_y^2 \end{bmatrix} \begin{bmatrix} E_x \\ E_y \\ E_z \end{bmatrix} = 0, \tag{9}$$

where $k_0 = \omega/c$ is the magnitude of wavevector and $c = 1/\sqrt{\varepsilon_0 \mu_0}$ the speed of light in vacuum. We now focus our attention on uniaxial media, with optical axis oriented along the $\hat{\mathbf{z}}$ direction, $\varepsilon_{xx} = \varepsilon_{yy} \equiv \varepsilon_\perp$ and $k_\perp = \sqrt{k_x^2 + k_y^2}$. The imposition of nontrivial solutions to Eq. (9) leads to the dispersion relation:

$$\left(k_\perp^2 + k_z^2 - \varepsilon_\perp k_0^2\right)\left(\frac{k_\perp^2}{\varepsilon_{zz}} + \frac{k_z^2}{\varepsilon_\perp} - k_0^2\right) = 0. \tag{10}$$

When set to zero, the two terms above correspond to a spherical and an ellipsoidal isofrequency surface in the k-space; the first describes waves polarized in the *xy* plane (*ordinary* or *TE waves*), the second waves polarized in a plane containing the optical axis (*extraordinary* or *TM waves*).

The situation changes substantially if we assume an extreme anisotropy, namely if one between $\varepsilon_\perp$ and ε_{zz} is negative. Media with such an optical signature are termed *indefinite* from the point of view of algebra [11], since their permittivity tensor represents an indefinite nondegenerate quadratic form, and exhibit a number of unconventional properties. Permittivity components with an opposing sign result in a hyperboloidal isofrequency surface for the extraordinary polarization – hence the physical denomination *hyperbolic* media. As a consequence, waves with arbitrarily large wavevectors retain a propagating nature, while in isotropic materials they become evanescent due to the bounded isofrequency contour [12]. The choice $\varepsilon_\perp > 0$, $\varepsilon_{zz} < 0$ corresponds to a two-fold hyperboloid, and the hyperbolic medium is called *dielectric* (with reference to its behavior in the *xy* plane) [13] or *Type I* [9]; the choice $\varepsilon_\perp < 0$, $\varepsilon_{zz} > 0$ describes a one-fold hyperboloid, namely a *metallic* or *Type II* medium. Fig. 1 shows the isofrequency surfaces and the dispersion relation for the two cases.

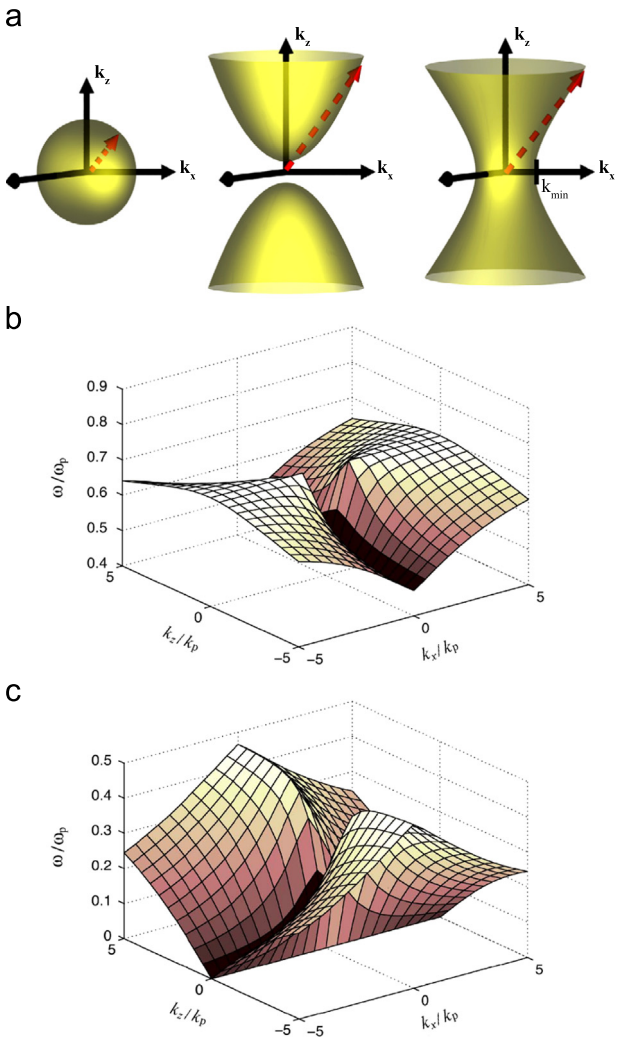

Fig. 1. (a) Isofrequency surface $\omega(k_x, k_y, k_z) =$ const. in the tridimensional k-space for an isotropic medium ($\varepsilon_\perp, \varepsilon_{zz} > 0$) and a hyperbolic medium with dielectric or Type I ($\varepsilon_\perp > 0, \varepsilon_{zz} < 0$) and metallic or Type II ($\varepsilon_\perp < 0, \varepsilon_{zz} > 0$) response. Dispersion relation $\omega(k_x, k_z)$ for a hyperbolic medium in the (b) dielectric and (c) metallic regime. k_p is the wavevector correspondent to the plasma frequency ω_p of the metallic constituent (see Section 2.2). (a) reproduced from Ref. [9], (b) and (c) from Ref. [10].

Another unique feature of a hyperbolic environment is the strongly directional light emission. The group velocity $\mathbf{v}_g(\omega) = \nabla_{\mathbf{k}}\omega(\mathbf{k})$ and the time-averaged Poynting vector $\hat{\mathbf{S}} = \frac{1}{2}\mathrm{Re}\{\mathbf{E} \times \mathbf{H}^*\}$, associated respectively with the directions of *propagation* and *energy flow* of light rays, are orthogonal to the isofrequency surfaces [10,11,14]. Let us consider a section of the metallic-type hyperboloid in the $k_x k_z$ plane, illustrated in Fig. 2. Except for a small region in proximity of the origin, the normals to the hyperbola coincide with those to its asymptotes, defined by

$$k_z = \pm\sqrt{-\frac{\varepsilon_\perp}{\varepsilon_{zz}}}k_\perp . \tag{11}$$

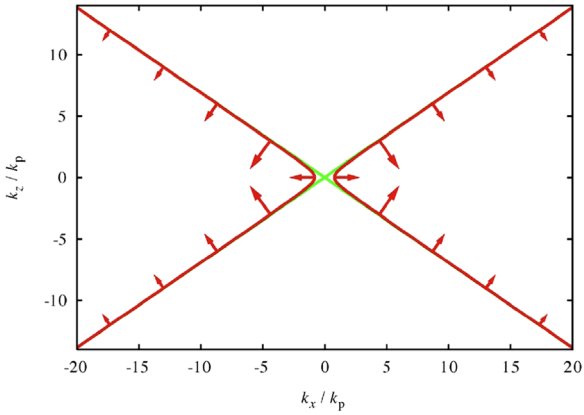

Fig. 2. Isofrequency contour in the k_x, k_z plane at $\omega = 0.2\omega_p$ for the metallic-type hyperbolic medium of Fig. 1(c). The group velocity is directed as the arrows and proportional to their magnitude, the green straight lines are the asymptotes given by Eq. (11). Reproduced from Ref. [10]. (For interpretation of the references to color in this figure caption, the reader is referred to the web version of this paper.)

Therefore, electromagnetic radiation and energy travel preferentially along a *cone*, with axis coincident with the optical axis $\hat{\mathbf{z}}$ and half-angle

$$\theta = \arctan\left(\sqrt{-\frac{\varepsilon_\perp}{\varepsilon_{zz}}}\right). \tag{12}$$

Such a spatial grouping of light is forbidden in conventional dielectric media, described by spherical or ellipsoidal isofrequency surfaces: in that case the normals point in all directions, resulting in isotropic emission patterns.

The peculiar anisotropic character does not manifest itself only in the bulk of hyperbolic media, but also at the interface with dielectrics, enabling negative refraction of energy [15,16]. With reference to Fig. 3, let us consider an isotropic material, where $\mathbf{k}$ and $\hat{\mathbf{S}}$ are parallel, in contact with a hyperbolic medium of the dielectric type ($\varepsilon_\perp > 0$ and $\varepsilon_{zz} < 0$). We want to determine the refraction of a TM-polarized plane wave (electric field in the xz plane), with x-component of the wavevector $k_x > 0$, impinging from the isotropic side on the interface between the two media, lying in the xy plane. The fact that in the anisotropic half-space k_x and k_z are connected by

$$\frac{k_x^2}{\varepsilon_{zz}} + \frac{k_z^2}{\varepsilon_\perp} = k_0^2, \tag{13}$$

namely $\mathbf{k}$ is constrained to the hyperbolic contour, and the conservation of the tangential component k_x, following from the absence of optical discontinuities in the xy plane, restrict the refracted wavevector to one between the dashed and the solid blue arrow in Fig. 3(a). Furthermore, the causality principle requires that $\hat{S}_z > 0$ (the energy flux has to be away from the interface) and only the solid blue arrow satisfies

$$\hat{S}_z = \frac{\hat{\mathbf{z}} \cdot \mathbf{k}}{\varepsilon_\perp} \frac{H_0^2}{2\omega\varepsilon_0} > 0. \tag{14}$$

This selected orientation implies that the wavevector, representing the propagation of phase fronts, undergoes positive refraction at the interface (Fig. 3(b)). If we evaluate instead the

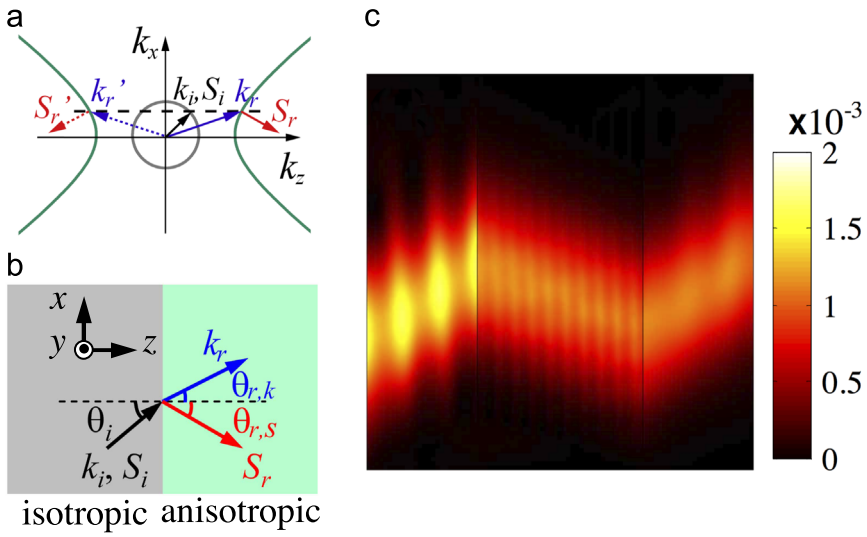

Fig. 3. (a) Isofrequency contour of an indefinite material with $\varepsilon_{xx} = 4.515$ and $\varepsilon_{zz} = -2.530$ (green hyperbola), and of an isotropic material (gray circle). Light incident from an isotropic medium, where the wavevector $\mathbf{k}_i$ and the Poynting vector $\mathbf{S}_i$ are parallel (black arrow), can generate in a hyperbolic medium two possible sets (solid and dashed arrows) of refracted wavevector (blue)/ Poynting vector (red), both satisfying Eq. (13) and the conservation of the k-component tangential to the interface. The physically correct one (b) is selected by invoking the causality principle. (c) Finite-element simulation showing negative refraction of a TM Gaussian beam at $\lambda_0 = 632.8$ nm through a slab of hyperbolic medium. The color bar represents the time-averaged Poynting vector. Reproduced from Ref. [15]. (For interpretation of the references to color in this figure caption, the reader is referred to the web version of this paper.)

tangential component of $\hat{\mathbf{S}}$,

$$\hat{S}_x = \frac{k_x}{\varepsilon_{zz}} \frac{H_0^2}{2\omega\varepsilon_0}, \tag{15}$$

it results <0, since the conserved quantity $k_x > 0$ while $\varepsilon_{zz} < 0$. This means that the sign of $\hat{S}_x$ flips across the interface (Fig. 3(b)), and hence that energy is negatively refracted when passing from an isotropic to a hyperbolic medium or viceversa (Fig. 3(c)).

2.2. Implementations

We now ask ourselves the question whether a natural material exists which possesses direction-dependent permittivities with opposing sign. Permittivity represents the macroscopic response of a system of charged particles to an externally applied electric field. A positive permittivity implies a polarization parallel to the field, and characterizes insulators. A negative permittivity, indicating an antiparallel polarization, is observed at infrared frequencies in dielectrics and semiconductors, in bands comprised between transverse and longitudinal phonons (Reststrahlen band) [17], and in systems described as free electron gases below the plasma frequency [18].

A difference in frequency between phononic modes parallel and perpendicular to the optical axis causes triglycine sulphate and sapphire to exhibit hyperbolic dispersion respectively in the low-terahertz ($250 < \lambda_0 < 268$ μm) and the mid-infrared (around 20 μm) range, while bismuth owes its 10-μm anisotropy window in the far-infrared ($53.7 < \lambda_0 < 63.2$ μm) range to direction-dependent effective masses [19]. Highly oriented pyrolytic graphite displays hyperbolic behavior in the

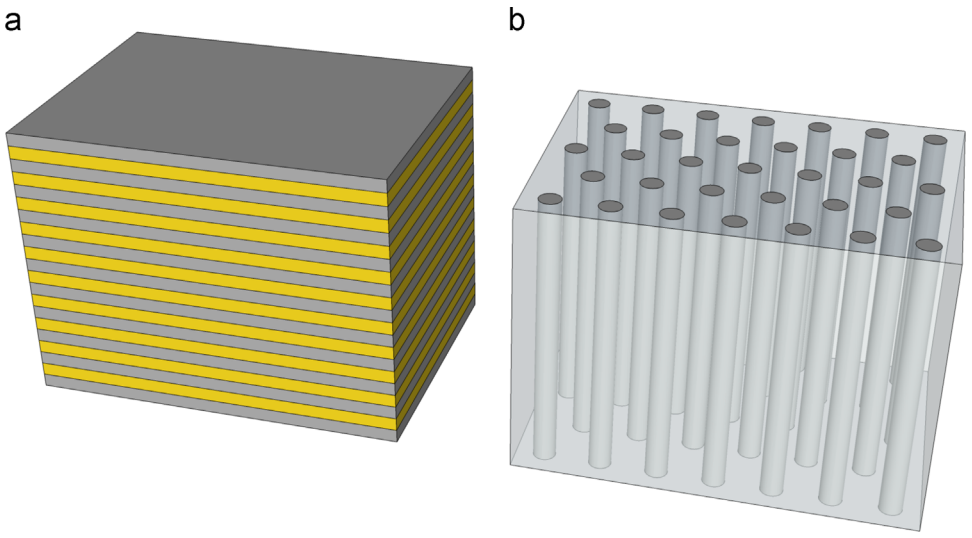

Fig. 4. Schematics of (a) a multilayer and (b) a nanowire hyperbolic metamaterial.

ultraviolet region, allowed by the free motion of electrons along parallel atomic layers, but its performance is limited by absorption losses [20]. Therefore, the available alternatives do not grant access to the visible range, and are too scarce to constitute a solid and versatile tool for applications.

In order to design a hyperbolic medium and customize its properties, one needs to artificially induce a negative permittivity in one or two spatial dimensions. The first attempt in this direction dates back to the late 1960s, when permittivity engineering was proposed by restricting to 1D the motion of a magnetized electron plasma by means of a constant magnetic field [21]. This approach, unpractical in terms of device portability and again limited in frequency, was overcome in the past decade thanks to progresses in nanofabrication, which allowed the confinement in less than three dimensions of the free electrons of metals. Currently, two structures have been shown to generate the desired kind of anisotropy: a stack of deep subwavelength alternating metallic and dielectric layers, termed *multilayer*, and a lattice of metallic nanowires embedded in a dielectric matrix, termed *nanowire array* (Fig. 4). The optical response of these discontinuous media can be homogenized via an effective medium theory (EMT), resulting in a hyperbolic effective permittivity tensor. The ML and the NW array constitute within such approximation *hyperbolic metamaterials*.[2] The physical mechanism that originates in the real implementations the properties discussed in Section 2.1 is the coupling of surface plasmons (in the ML case) or localized surface plasmons (in the NW case) of individual metallic/dielectric interfaces [4,5]; we will delve deeper in this aspect in the following section.

2.2.1. Multilayer

The effective parameters in the limit of infinitesimal layer thickness for a ML parallel to the *xy* plane, originally derived by Rytov [22] and later reobtained with the characteristic matrix formalism by Wood et al. [10], are

$$\varepsilon_{xx} = \varepsilon_{yy} = p\varepsilon_m + (1-p)\varepsilon_d \tag{16}$$

[2]Photonic crystals exhibit a periodicity analogous to that of MLs and NW arrays, but are not metamaterials as they cannot be represented by effective bulk parameters.

$$\varepsilon_{zz} = \left(\frac{p}{\varepsilon_m} + \frac{1-p}{\varepsilon_d} \right)^{-1}, \tag{17}$$

where the *filling ratio* $p = t_m/(t_m + t_d)$ is the volume percentage of metal in a unit cell or *period*, constituted of a dielectric layer and a metallic layer with thicknesses t_d and t_m and permittivities ε_d and ε_m. In general, ε_d and ε_m are complex quantities exhibiting temporal dispersion (i.e. they depend on the angular frequency ω), and so are ε_{xx} and ε_{zz}. As we chose the '+' sign in the plane wave time-dependence $e^{i\omega t}$ (Section 2.1), our sign convention for permittivity will be $\varepsilon = \varepsilon' - \varepsilon''$. The real part ε', <0 for ε_m and >0 for ε_d, accounts for polarization response, while the imaginary part ε'', >0 for both ε_d and ε_m, models the dissipative (or "ohmic") losses in the material. The real and imaginary parts of the effective parameters of a Ag/SiO_2 ML are plotted in Fig. 5 for two different filling ratios. As p and ω are varied, the medium described by Eqs. (16) and (17) can not only exhibit Type I or Type II hyperbolic character, but also behave as an effective dielectric ($\varepsilon_{xx}, \varepsilon_{zz} > 0$) or an effective metal ($\varepsilon_{xx}, \varepsilon_{zz} < 0$), as summarized in the optical phase diagrams of Fig. 6 [9,23]. A proper selection of parameters allows access to the epsilon-near-zero (ENZ) regime [24].

ML HMMs are fabricated by electron-beam or sputter deposition in vacuum of both the metallic and non-metallic constituents. Fig. 7 shows a most recently demonstrated ML HMM of superior quality, fabricated with sputtering technology. The choice of materials depends on the target spectral range, on losses and on the impedance match. The latter requires that the absolute values of ε_d' and ε_m' do not differ by more than an order of magnitude, in which case radiation coming from the dielectric side is reflected instead of propagating. The plasma frequencies of Ag and Au fall in the ultraviolet region, at 2224.3 and 2151.7 THz (9.2 and 8.9 eV) [18]. Below those values, the real part of permittivity of such plasmonic metals becomes negative, and increases in magnitude as frequency progressively decreases. Throughout the ultraviolet and visible regions, on one hand losses are limited, and on the other hand the relatively small ε_m' can be impedance-matched with the ε_d' of poorly absorbing dielectrics such as Al_2O_3 and TiO_2. When moving to the infrared region, the real part of permittivity in metals becomes so negative that it causes an impedance mismatch with any other media. Therefore, Ag and Au need to be replaced with semiconductors, whose plasma frequency falls in the infrared region and can be controlled by doping. Accordingly, intrinsic semiconductors play the role of dielectrics [25].

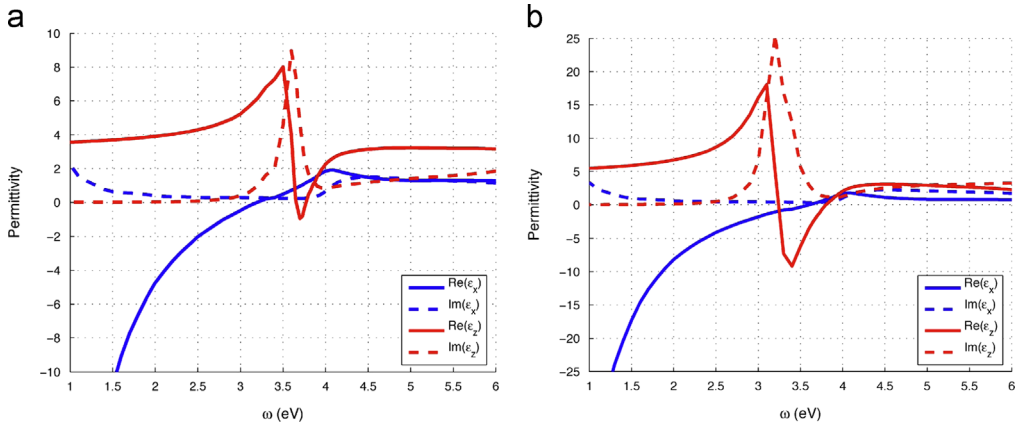

Fig. 5. Real and imaginary parts of the in-plane ε_x and perpendicular ε_z permittivity components for a Ag/SiO_2 multilayer with filling ratio: (a) $p=0.4$ and (b) $p=0.6$. Reproduced from Ref. [10].

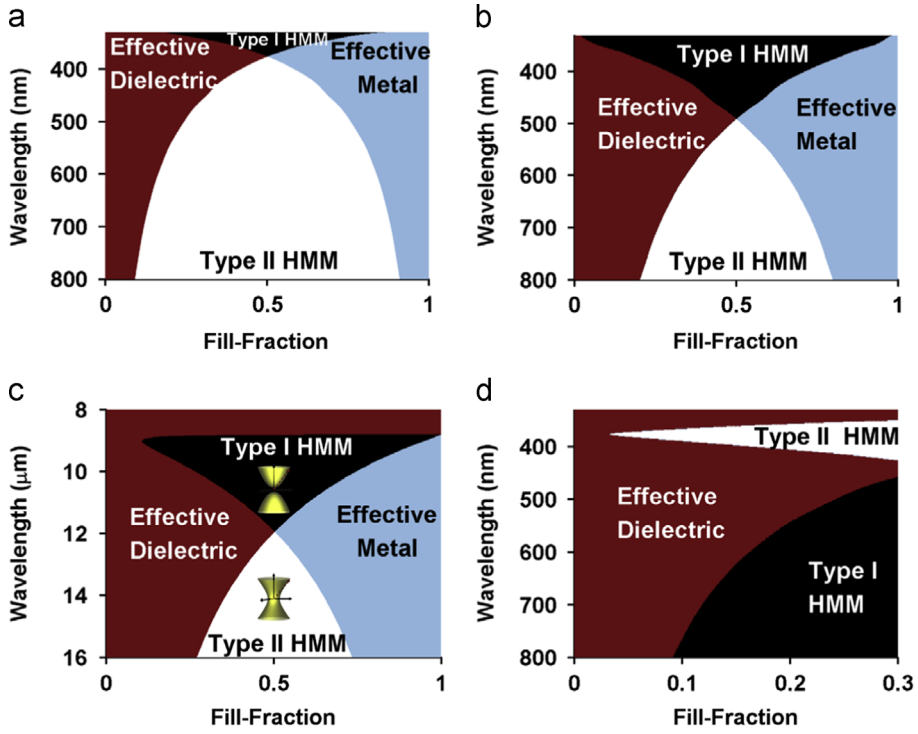

Fig. 6. Optical phase diagrams for (a) a Ag/Al_2O_3 multilayer system, (b) a Ag/TiO_2 multilayer system, (c) an AlInAs/InGaAs multilayer system and (d) Ag nanowires in an Al_2O_3 matrix. Reproduced from Ref. [9].

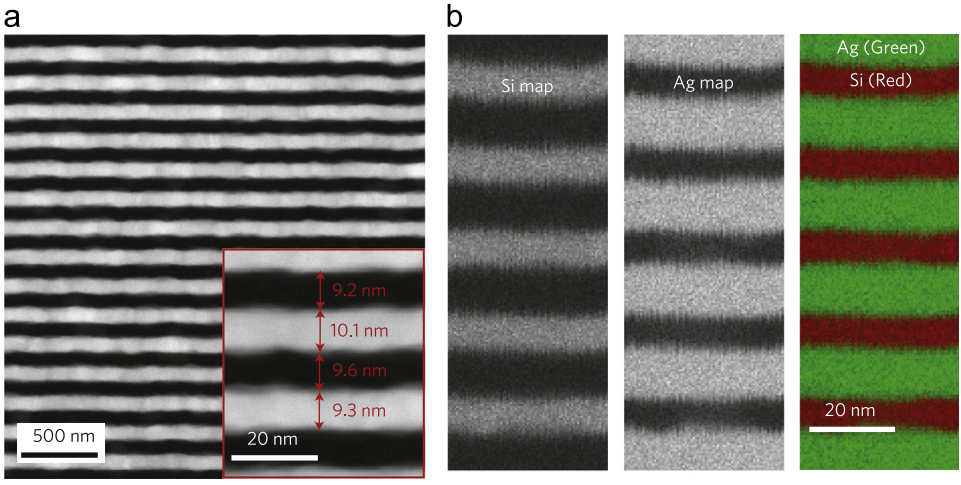

Fig. 7. (a) Dark-field STEM images of the cross-sections of Ag/Si multilayers, deposited by DC magnetron sputtering, showing well-formed periodic lattice structures (filling ratio $\rho = 0.5$, period 20 nm). The white color corresponds to Ag, the black one to Si. (b) Element mapping for the constituent materials (Si and Ag), verifying the established multilayer lattice with some minor diffusion of Ag into Si. Reproduced from Ref. [26].

Alternative plasmonic materials for optical applications have been proposed to operate in the near-infrared and the mid-infrared range [18,27], while graphene was predicted to induce a tunable hyperbolic response at THz frequencies [28–32]; SiC/SiO_2 layered media, which derive their anisotropy from phononic resonances [33], are currently being investigated for thermal engineering of the near field [34,35]. Table 1 collects the experimentally demonstrated material combinations that lead to MLs with hyperbolic properties.

We observe that Eqs. (16) and (17) only depend on the filling ratio p, disregarding the period. This is because such approximations are obtained in the limit of vanishing thicknesses of the constituent layers. Strictly speaking that situation should be treated in a different way, since quantum size effects induce in metals a spatial dispersion, in addition to the ordinary temporal dispersion (so that ε_m becomes a function not only of the frequency ω, but also of the wavevector $\mathbf{k}$), which alters their hyperbolic character [48–55]. We shall analyze the implications of extremely reduced sizes in Section 4. As a rule of thumb, in metal layers thicker than 5 nm spatial dispersion can be neglected. A practical criterion for Eqs. (16) and (17) to be applicable is that the ML period must be much smaller than the wavelength of operation (thereby preventing radiation from perceiving optical discontinuities); a more accurate description, that includes the dependence on layer thickness in a second order term, was adopted in [38]. In real media, fabrication poses a limit to the number of periods that can be stacked while preserving an actual ML structure; a total of eight layers was estimated to be the threshold to observe the predictions of the EMT [9], although as little as six layers were shown to achieve an effective hyperbolic behavior [13,47].

2.2.2. *Nanowire array*

To determine EMT parameters for NW media is not as straightforward as for MLs, since the homogenization adopted strongly depends on the frequency range of interest. Spatial dispersion cannot be neglected [56–58] and leads to non-hyperbolic isofrequency contours, except in the optical region, where it is reduced by the kinetic inductance and by the losses of the metallic

Table 1
Material combinations for the fabrication of multilayer hyperbolic metamaterials.

Range	Materials	Period (nm)	p	N. of periods	Reference
UV	Ag/Al_2O_3	70	0.5	8	[36]
Visible	Au/Al_2O_3	38	0.5	8	[37–39]
	Au/Al_2O_3	40	0.5	8	[40]
	Au/Al_2O_3	43	0.35	10	[41]
	Au/TiO_2	48	0.33	4	[42]
	Ag/PMMA	55	0.45	10	[43]
	Ag/LiF	75	0.4	8	[43]
	Ag/MgF_2	50	0.4	8	[43]
	Ag/MgF_2	60	0.42	7	[44]
	Ag/TiO_2	31	0.29	5	[23]
	Ag/Ti_3O_5	60	0.5	9	[45]
	Ag/SiO_2	30	0.5	3	[13]
	Ag/Si	20	0.5	15	[26]
IR	AlInAs/InGaAs	160	0.5	50	[25]
	Al:ZnO/ZnO	120	0.5	16	[46]
	Ag/Ge	50	0.4	3	[47]

constituent [59,60]. With a z-axis orientation parallel to the wires, the effective permittivity tensor takes the form [15,62,61,63]:

$$\varepsilon_{xx} = \varepsilon_{yy} = \frac{[(1+p)\varepsilon_m + (1-p)\varepsilon_d]\varepsilon_d}{(1-p)\varepsilon_m + (1+p)\varepsilon_d} \tag{18}$$

$$\varepsilon_{zz} = p\varepsilon_m + (1-p)\varepsilon_d, \tag{19}$$

where this time p is the percentual area occupied by NWs in an xy section of the medium. As for ML HMMs, the response of NW media can be tuned to different regimes by varying ω and p (Fig. 6(d)); an example of effective parameters for two typical filling ratios is shown in Fig. 8.

Due to the extremely high aspect ratio, most of the practical NW HMMs are fabricated by electrochemical deposition of Ag or Au inside a self-assembled porous alumina (Al_2O_3) template [16,61,64–66]. The geometrical features of such a matrix, prepared by electrochemical anodization of Al, can be finely tailored via multiple fabrication parameters or through extra steps (such as focussed-ion-beam (FIB) pre-patterning), ensuring the formation of ordered and extremely dense pores (Fig. 9). Table 2 reports the characteristic sizes of Al_2O_3 templates, together with other possible material choices for the host matrix. Arrays of carbon nanotubes in the metallic state have been proposed as an alternative to the template-NW scheme, thanks to their capability to quench spatial dispersion and the high degree of control of their growth [67].

The chemical processes and the self-organizational mechanisms through which porous templates are manufactured confer on NW HMMs an advantage over their ML counterparts, in

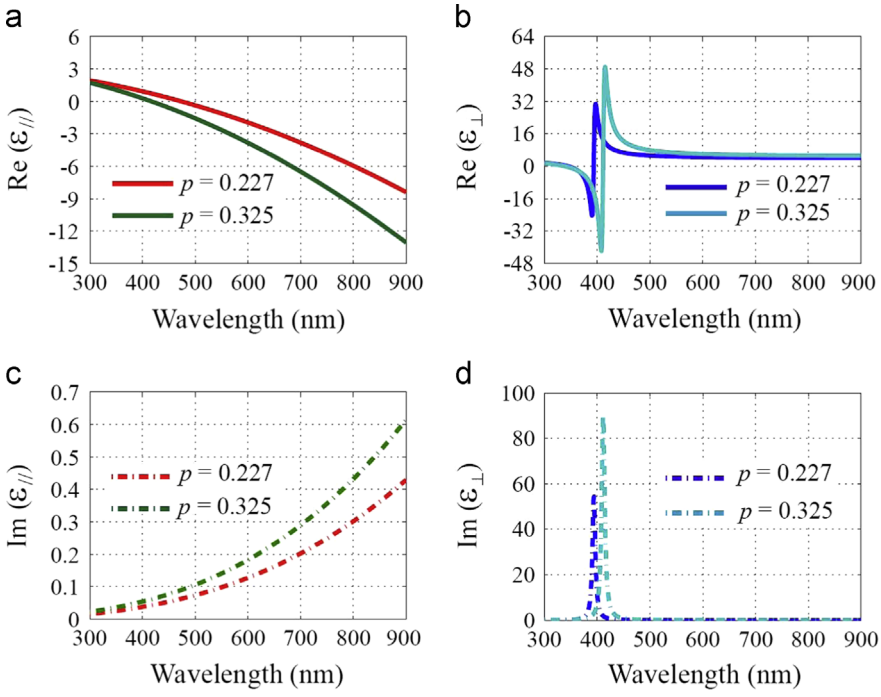

Fig. 8. Effective permittivities for Ag nanowires embedded in an Al_2O_3 matrix with two different filling ratios p. (a) and (b) plot the real part of the permittivity parallel and perpendicular to the nanowire, respectively. (c) and (d) are the corresponding imaginary parts. Reproduced from Ref. [15].

terms of ease and cost of fabrication. Besides their potential application in imaging as negatively refracting materials [15,16,68] and in spontaneous emission engineering [69], these media have been demonstrated to be superior biosensors [70]. A guided mode can be excited under resonant conditions in an assembly of Au nanorods, either embedded in an Al_2O_3 template or free-standing, in contact with the liquid to analyze. In analogy to conventional SPP-based devices, an increase in the refractive index causes a redshift of the resonance, but with a sensitivity two order of magnitude higher (32,000 nm per RIU). In addition, the probe depth is large (500 nm), and the discontinuous porous nanotexture of the nanorod matrix allows degrees of freedom in the experimental design unaccessible with uniform plasmonic films.

3. Applications

3.1. High-resolution imaging and lithography

Light emitted or scattered off an object can be thought of as a Fourier superposition of plane waves. Low k-vector components of the spatial spectrum encode large geometric features, while high k-vectors describe finer details. In an isotropic medium, characterized by bounded

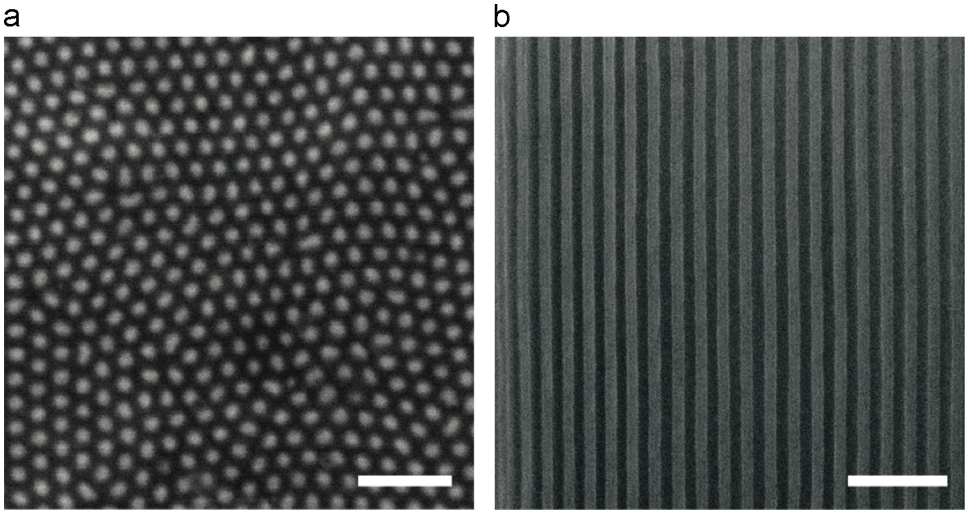

Fig. 9. SEM images of the earliest experimentally demonstrated nanowire hyperbolic metamaterial, consisting of Ag nanowires electrochemically plated in an anodic aluminum oxide (AAO) template. (a) Top view and (b) cross section of the nanowires (light gray regions), with a diameter of 60 nm and a center-to-center distance of 110 nm. *Scale bars*: 500 nm. Reproduced from Ref. [16].

Table 2
Main parameters of nanoporous matrices made of Al_2O_3, $A^{III}B^{V}$ semiconductor compounds and porous-Si by electrochemical etching. Reproduced from Ref. [60].

Material	Pore diameter	Pore wall thickness	Thickness of matrices
Al_2O_3	20–70 nm	15–30 nm	>2 μm
$A^{III}B^{V}$	20–500 nm	10–100 nm	>150 μm
Si	10 nm–several μm	10 nm–several μm	>400 μm

isofrequency contours, momenta larger in magnitude than k_0 correspond to evanescent waves: therefore, they are forbidden from propagating into the far-field, which results in loss of information. This phenomenon, known as diffraction limit, causes resolution in conventional imaging devices to be limited to distances $R > (0.61\lambda)/NA$ (Rayleigh criterion), where NA is the numerical aperture of the imaging system [12].

The technological challenge for high-resolution microscopy is to recover in the far-field the evanescent components of the spectrum [71]. Different approaches have been proposed based on near-field optical scanning [72], fluorescent imaging [73] or stochastic optical reconstruction imaging [74], with the common disadvantage of low throughput and speed. An extremely thin Ag slab can act as a superlens, which enhances evanescent waves via resonant excitation of surface plasmons [75–77]. The non-propagating nature of these components stays unaltered while they are transmitted through the metallic medium, so that a coupling element is ultimately required to scatter them into the far-field.

HMMs offer a completely new paradigm to tackle the problem [78]. Their unique anisotropic dispersion naturally supports high k-vector components without relying on resonant mechanisms (intrinsically limited in frequency, and detrimental to image formation due to absorption losses), and makes them ideal candidates not only to read but also to write nanoscale information.

Fundamental phenomena such as negative refraction [16,79–82] and partial focusing of radiation [13,83–85] make clear the impact of HMMs on the field of imaging. The experimental efforts to shape hyperbolic media into imaging devices resulted in the invention of the hyperlens, that we discuss together with its numerous developments and implications in the following two subsections.

3.1.1. Hyperlens

Any plane wave illuminating an object can be written as an expansion of cylindrical waves:

$$\exp(ikx) = \sum_{m=-\infty}^{\infty} i^m J_m(kr)\exp(im\phi), \tag{20}$$

where i is the imaginary unit, k is the magnitude of the wavevector, $J_m(kr)$ denotes the Bessel function of the first kind, m is the angular momentum mode number of the cylindrical wave and r, ϕ are cylindrical coordinates (distance from the origin and azimuthal angle) [86]. In an ordinary isotropic medium, the radial component of the electric field decays exponentially at the origin as m becomes higher (Fig. 10(a)). The conservation of angular momentum, $m = k_\theta r$, implies indeed that a progressively smaller distance r from the center corresponds to a larger tangential wavevector component k_θ. In order for the isotropic dispersion relation

$$k_r^2 + k_\theta^2 = \varepsilon\frac{\omega^2}{c^2} \tag{21}$$

to be satisfied, the arbitrary growth of k_θ necessarily results in an imaginary radial component k_r, and therefore in a mode evanescent near the origin. On the other hand, in a hyperbolic medium with strong *cylindrical anisotropy* – radial permittivity $\varepsilon_r < 0$, tangential permittivity $\varepsilon_\theta > 0$ – k_r and k_θ are connected by

$$\frac{k_r^2}{\varepsilon_\theta} - \frac{k_\theta^2}{|\varepsilon_r|} = \frac{\omega^2}{c^2}. \tag{22}$$

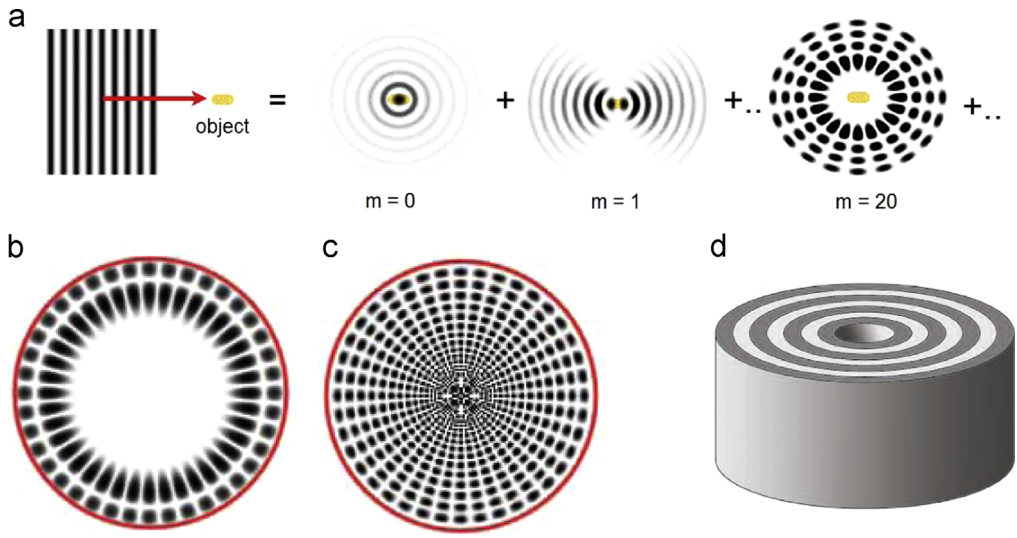

Fig. 10. (a) Cylindrical wave expansion of a plane wave scattered by a target (yellow object). The regions of high electric field intensity are shown in black, those of low intensity in white. High angular momentum state (b) in an isotropic dielectric cylinder and (c) in a cylinder made of an effective hyperbolic medium with $\varepsilon_r < 0$ and $\varepsilon_\theta > 0$. (d) Possible realization of a hyperlens, consisting in alternating concentric metallo/dielectric layers. Reproduced from Ref. [86]. (For interpretation of the references to color in this figure caption, the reader is referred to the web version of this paper.)

This dispersion is unbounded, so that now as k_θ increases toward the center, k_r also increases, staying real for any value of r and m. As a consequence, high-m modes are allowed to reach the origin, and access small object features. The comparison between the field distribution in an isotropic medium (Fig. 10(b)) and in a metamaterial with cylindrical hyperbolic anisotropy (Fig. 10(c)) shows that in the second case not only the mode penetrates toward the center, but also the distance between the field nodes at the core gradually decreases, enabling sub-wavelength probing of spatial details.

A practical configuration that exploits the cylindrical dispersion (22) is obtained by bending a flat multilayer into a hollow core cylinder like the one in Fig. 10(d). This device can act as a hyperlens, in that it turns sub-wavelength objects inscribed on its inner walls with radius R_{in} into magnified images on the outer surface with radius R_{out}. Such behavior is made possible by two simultaneous mechanisms. The first is the propagation of high k-vector waves, which the hyperbolic environment prevents from becoming evanescent. The second is the compression of the tangent wavevector component k_θ as the waves travel along the radial direction, dictated by the angular momentum conservation ($k_\theta \sim 1/r$). This near-to-far field conversion of information from the internal to the external boundary of the cylinder results in a magnification factor simply given by the ratio R_{out}/R_{in} [86,87].

The first experimental implementation of a hyperlens was optimized for ultraviolet frequencies [36,88]. It consisted of a curved stack of 16 alternating Ag and Al_2O_3 layers, each 35 nm thick, deposited by electron-beam evaporation on a half-cylindrical quartz mold (Fig. 11). Sub-diffraction limited objects were inscribed into a 50-nm-thick Cr layer located at the inner surface, and – upon illumination at the wavelength $\lambda_0 = 365$ nm – magnified at the outer boundary of the hyperlens, where they were detected via a conventional imaging system with $\lambda_0/1.4$ (corresponding to 260 nm) resolution (Fig. 12(a) and (b)). A control experiment showed that in

the absence of the hyperlens the same objects could not be resolved by the same apparatus (Fig. 12(c) and (d)). The device was able to image features as closely spaced as 125 nm, therefore achieving a $\lambda_0/2.92$ resolution [88].

This cylindrical prototype of hyperlens is impractical for imaging applications since its magnification is limited to one dimension. The use of a spherical geometry in combination with a different material choice allowed 2D resolution improvement in the visible range [45]. The spherical hyperlens was fabricated by conformal deposition of 18 alternating layers of Ag and Ti_3O_5, all of equal thickness 30 nm, onto a hemi-spherical quartz mold (Fig. 13). A high-index dielectric material such as Ti_3O_5 matches the larger magnitude of the permittivity of Ag in the visible range, as compared to the ultraviolet range, moving accordingly the operational wavelength to that region [89]. Objects with different shapes and configurations were inscribed in the inner side of the hyperlens and illuminated at $\lambda_0 = 410$ nm. Two apertures separated by 160 nm generated images with a 333 nm spacing, corresponding to an averaged magnification ratio of 2.08 (Fig. 14). The performance of the spherical hyperlens is limited by defects in fabrication, resulting in loss of concentricity of the layers and in a position-dependent magnification, and by the curved outer surface of the device, which causes distortion in the subsequent far-field image.

Besides the disadvantage just discussed, a curved geometry, based on which the first hyperlens predictions were formulated [86,93,94], is hard to implement in biological applications. As an alternative, planar configurations were proposed that replaced both the inner and the outer (Fig. 15(a)) of just the outer (Fig. 15(b) and (c)) curved surface with parallel planes by redesigning the layer shape, or more generally the space properties, via transformation optics [90,91,95,96]. A hybrid-superlens hyperlens, where an object on a flat input surface is imaged at a curved output boundary, was recently investigated (Fig. 15(d)) [92]. An inherent limitation of strongly anisotropic media is the huge impedance mismatch at the interface with low-index dielectrics. To mitigate the in-coupling and out-coupling reflection losses of the hyperlens one can customize $\overline{\overline{\boldsymbol{\mu}}}$ and $\overline{\overline{\boldsymbol{\epsilon}}}$ through transformation optics: a radius-dependent permeability allows simultaneous match at both interfaces, while a nonmagnetic medium can only act either on the

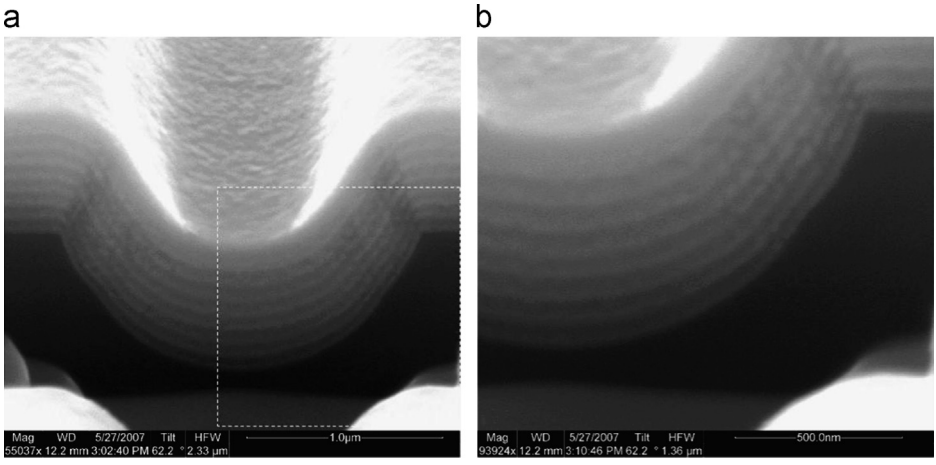

Fig. 11. (a) SEM image of the cross section of the cylindrical hyperlens. Bright and dark layers correspond to Ag and Al_2O_3 respectively, while the topmost thick and bright layer is Cr. (b) Zoomed detail of the white dashed square in (a). Reproduced from Ref. [88].

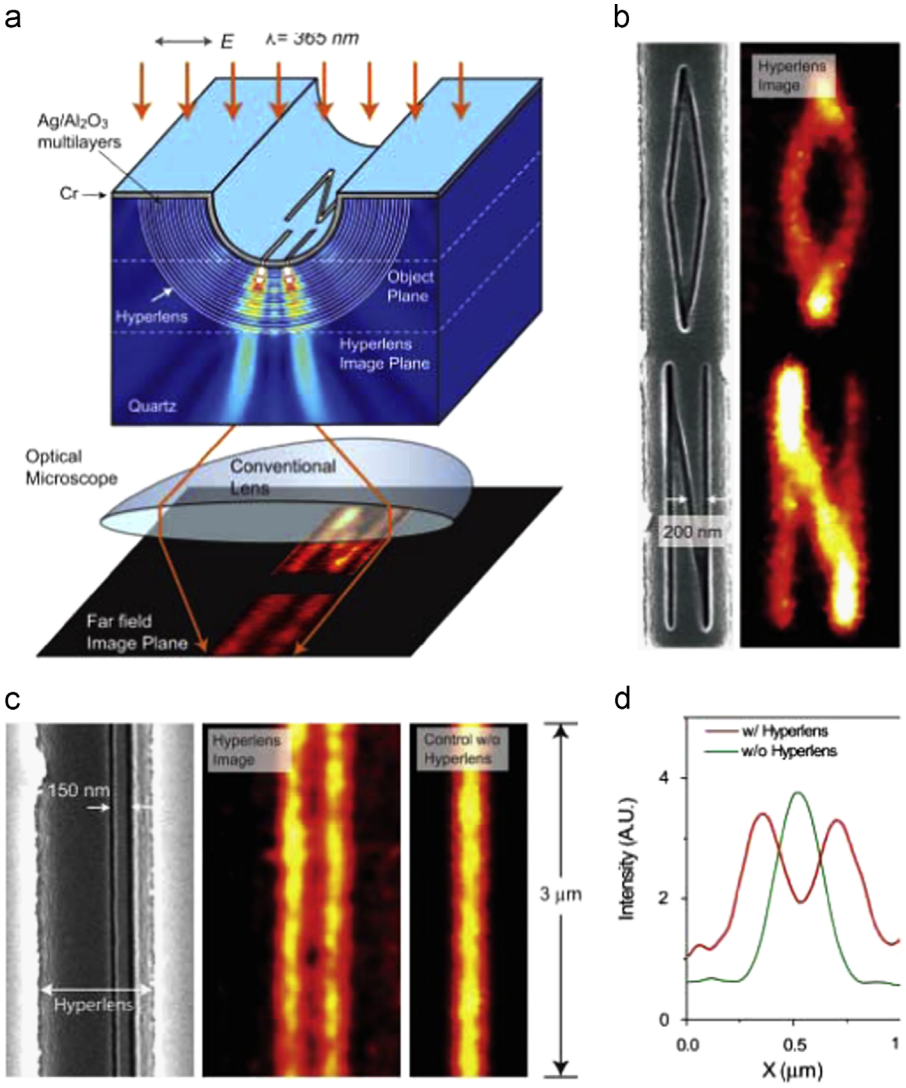

Fig. 12. (a) Schematic of the cylindrical hyperlens with a numerical simulation showing imaging of sub-diffraction limited objects. (b) Arbitrary object (the word "ON") imaged with sub-diffraction resolution. The width of the lines composing the object is about 40 nm. (c) Left to right: SEM top view of a 150-nm-spaced line pair object fabricated near the inner surface of the hyperlens, magnified image obtained with the hyperlens that clearly resolves the object and diffraction-limited image from a control experiment without the hyperlens. (d) Averaged cross-section of the object in (c), imaged with (red curve) and without (green curve) the hyperlens. Reproduced from Ref. [36]. (For interpretation of the references to color in this figure caption, the reader is referred to the web version of this paper.)

inner or on the outer boundary (Fig. 16(a) and (b)) [97]. A complementary approach to suppress scattering consists in immersing the hyperlens into high-index liquids (Fig. 16(c) and (d)) [89]. In order for a device to behave as a conventional lens, it should be capable to focus plane waves. This is forbidden to hyperlenses, since they lack a phase compensation mechanism [87].

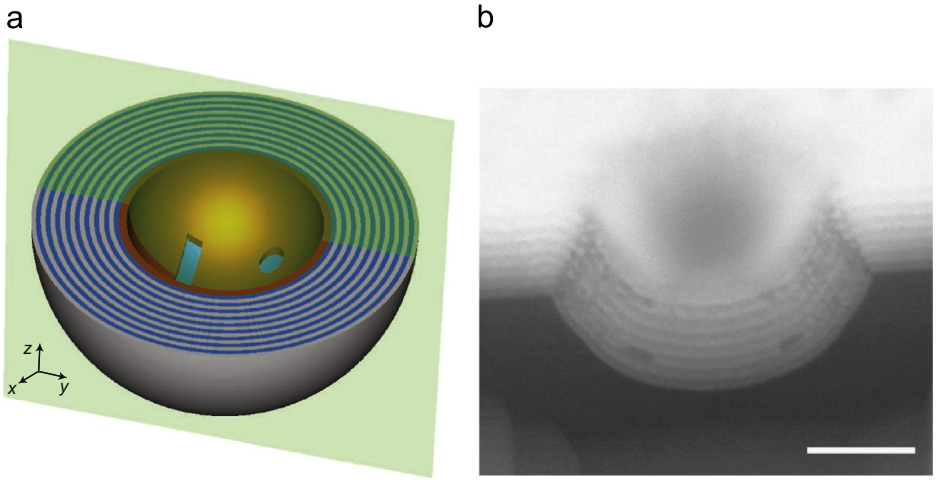

Fig. 13. (a) Schematic of the spherical hyperlens: 9 Ag (30 nm)/Ti_3O_5 (30 nm) periods, and a 50-nm Cr layer with two inscribed sample objects. (b) SEM image of the cross section of the spherical hyperlens, scale bar: 500 nm. Reproduced from Ref. [45].

Metalenses realizing the Fourier transform function were designed by providing with such a mechanism a slab of hyperbolic medium [98–100].

Absorption losses due to the metallic constituent are ineliminable, but can be circumscribed by increasing the percentage of dielectric or shifting the operating range to longer wavelengths [89]. A major source of nonideality in the experimentally demonstrated hyperlenses are fabrication imperfections, which can either be incorporated in theoretical models [101] or reduced at the manufacture stage with rolled-up technology [102–105].

Recent works studied a nonlinear hyperlens [106], a tunable hyperlens [32], and a hyperbolic metamaterial lens with hydrodynamical nonlocal response [54]. In the first, dielectric layers with high Kerr-type nonlinearity were introduced to minimize diffraction inside a hyperlens, allowing longer propagation distances and broadband operation in the ultraviolet region. In the second, the metallic layers of a cylindrical hyperlens were replaced with single sheets of graphene [31,107].

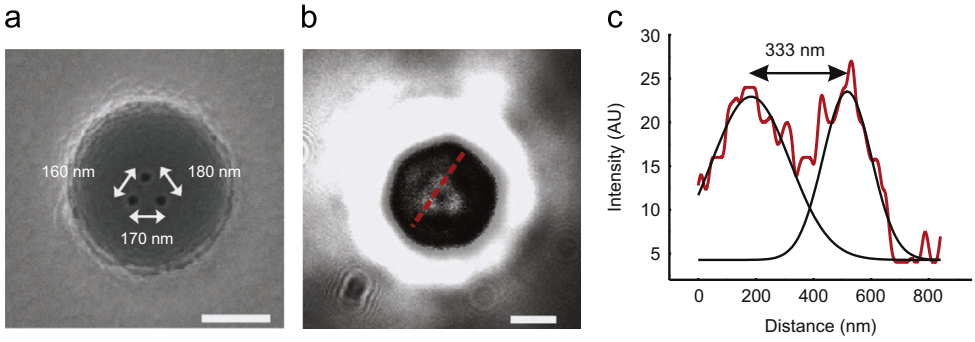

Fig. 14. (a) SEM image of three dots positioned triangularly with gaps of 180, 170 and 160 nm on the inner side of the spherical hyperlens. (b) Image and (c) cross-sectional analysis along the red dashed line of the object after being magnified. Scale bar in (a) and (b) is 500 nm. Reproduced from Ref. [45]. (For interpretation of the references to color in this figure caption, the reader is referred to the web version of this paper.)

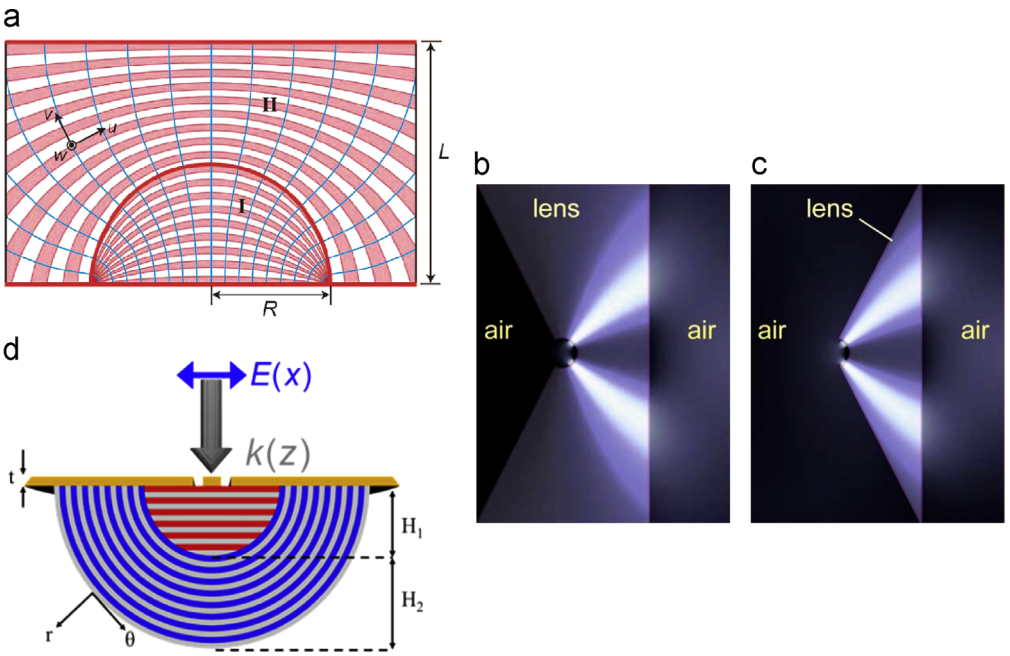

Fig. 15. (a) Schematic of an optical transformer consisting of two domains of alternating curved layers of metal (pink) and semiconductor (white). The light flows along the *v*-axis (curved blue lines), and the interfaces between the layers comply with the *u*-axis. (b) Magnetic field map inside a 3/4-body and (c) a 1/4-body hyperlens with flat output surface. (d) Schematic of the hybrid-superlens hyperlens. (a) reproduced from Ref. [90], (b) and (c) from Ref. [91], (d) from Ref. [92]. (For interpretation of the references to color in this figure caption, the reader is referred to the web version of this paper.)

The plasmonic response of this material can be dynamically manipulated in the THz region by controlling the chemical potential with an external bias voltage [108]: at a fixed frequency, the effective permittivities of a curved ML were tuned until they entered the desired hyperbolic regime. In the last study, the focussing properties of a slab of ML HMM were shown to depend on the metal permittivity model – nonlocal versus local – adopted: such system was therefore indicated as a potential candidate to test the validity of the hydrodynamic nonlocal theory.

The ability of detecting and manipulating sub-wavelength information is not a prerogative of ML implementations, but is also attainable with a NW geometry [60]. Wires can transport over a few wavelengths low k-vector information thanks to plasmonic resonances, a phenomenon known as canalization [109]. This corresponds to a superlensing behavior, which includes magnification if the wire arrangement is made divergent ("tapered configuration") instead of parallel [110], and is effective at THz or lower frequencies [111–113]. The hyperbolic properties of NW HMMs, that emerge in the infrared and the visible range, enable negative refraction [16], and therefore image focussing inside and outside a slab of such media [15,68]. Transport at telecom wavelengths (1510–1580 nm) of features as small as $\lambda_0/4$ over a distance $>6\lambda_0$ was demonstrated in a Au/Al_2O_3 NW HMM [114]. The quasi-TEM collective mode that guided the image was mostly localized in the dielectric matrix (pore diameter 12 nm, pore-to-pore average spacing 25 nm), which minimized the absorption losses. In addition, bottom-up grown templates allow the imaging of large areas, as compared with those available to hyperlenses. However, the lack of a magnification mechanism required a near-field scanning optical microscope (NSOM) to detect the transmitted image (Fig. 17), which impedes the integration of this

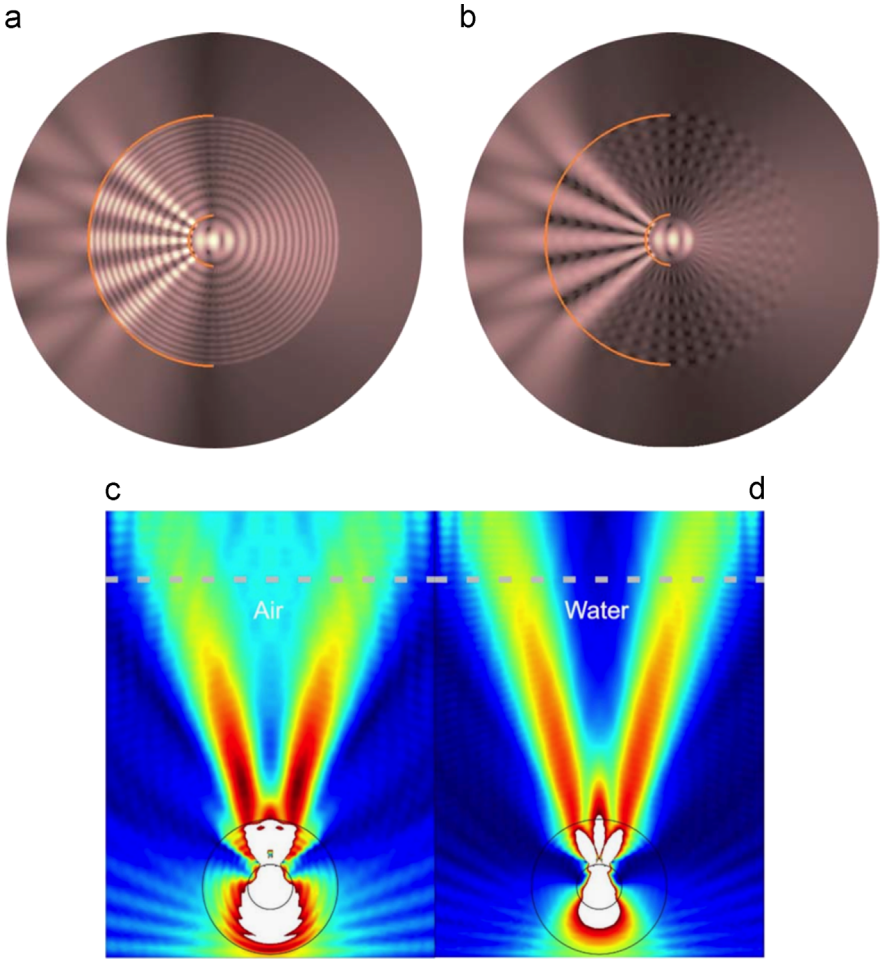

Fig. 16. Magnitude of the *H*-field for a cylindrical hyperlens designed to be impedance-matched (a) at the internal and (b) at the external interface. Normalized *H*-field distribution in a cylindrical hyperlens immersed in (c) air and (d) water. (a) and (b) reproduced from Ref. [97], (c) and (d) from Ref. [89].

technology in far-field devices. To the best of our knowledge, the performance of the ML-based hyperlens – diffraction-limited image transport and retrieval in the far field, entirely ascribable to bulk hyperbolic properties – has not been equaled with NW HMMs at optical frequencies.

3.1.2. Nanolithography

The diffraction limit poses a constraint not only on object details detectable with far-field equipment, but also on the resolution of patterns written by photolithography. In order to define sub-wavelength features, such a cost-effective and high-throughput technique is replaced by alternative forms of lithography, based for instance on electron-beam, focussed-ion-beam or imprint, that involve expensive machines and/or cleanroom processing.

A different solution consists in utilizing HMMs to miniaturize far-field information. This approach still relies on conventional photo-lithographic procedures, but wave propagation

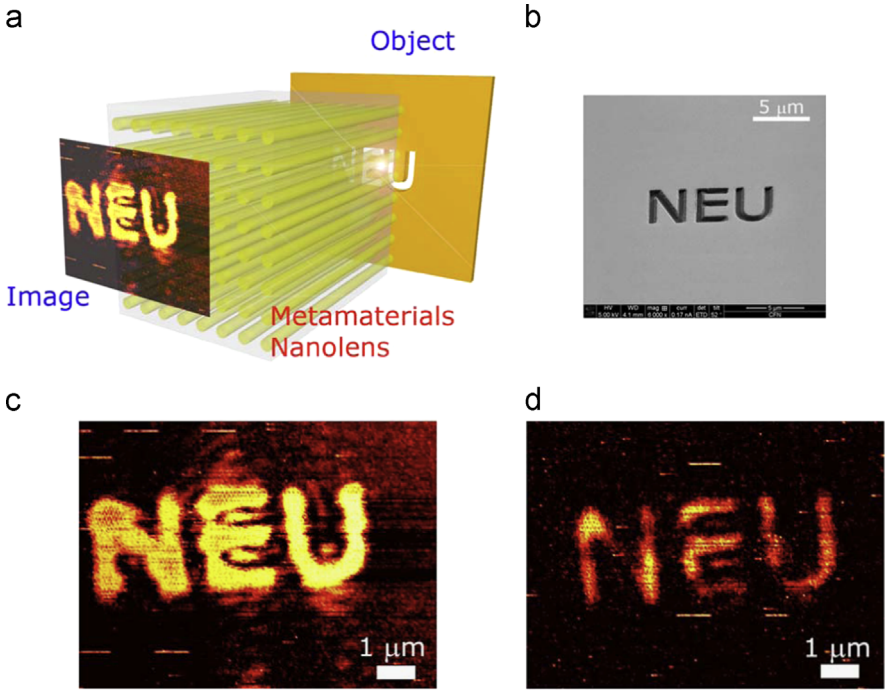

Fig. 17. (a) Schematic of sub-wavelength image transport with a NW HMM at $\lambda_0 = 1550$ nm. (b) SEM image of the "NEU" letters milled in 100-nm-thick Au film. The letters have 600-nm-wide arms (0.4 λ_0). (c) NSOM scan of the source object in the near-field. (d) NSOM scan of the corresponding image by the NW HMM at the output surface. Reproduced from Ref. [114].

through an anisotropic space enables ratios between the transferred image and the object smaller than 1:1. A Ag/SiO_2 ML slab was proposed to generate sub-diffraction-limited patterns from traditional 1D or 2D diffraction-limited masks. [115]. TM-polarized light at the wavelength of $\lambda_0 = 405$ nm was shone on a 1D mask with period $\Lambda = 400$ nm (Fig. 18(a)). The ML supported exclusively the propagation of those waves with tangential wavevector larger than nk_0 (n: refractive index of the medium on the transmission side of the grating); furthermore, its spatial frequency pass band could be tuned with design parameters to allow only one diffraction order ($\pm m$-th order) from the mask. The superposition of diffracted waves of the selected $\pm m$-th order formed on the other side of the slab a sub-diffraction-limited pattern with period $\Lambda/2m$. Specifically, the choice $m = 3$ resulted in a 6-fold miniaturization of the mask profile.

The hyperlens also exhibits writing capabilities, exploitable by simply reversing its direction of operation: a diffraction-limited pattern defined on the outer surface of radius R_{out} can be reduced to a sub-diffraction-limited one on the inner side of radius R_{in} by virtue of tangential wave vector de-compression, with a de-magnification given by the ratio R_{in}/R_{out} [116]. Finite element simulations (Fig. 18(b)) showed that a Ag/Al_2O_3 cylindrical hyperlens operating at $\lambda_0 = 375$ nm transforms a 1D mask of openings with a period 280 nm and width 140 nm in a pattern with a period 40 nm. This corresponds to a reduction factor of 1/7, which matches the radii ratio 120 nm/840 nm. To obtain flat input and output planes, the hyperlens can be polished as in Fig. 18(c). The linear reduction achieved is $x_i/x_o = (R + D)/R$, where R is the radius of the inner surface of the original hyperlens, and D is the thickness of the flat hyperlens. Currently, none of the alternative lithography schemes discussed has seen experimental implementation.

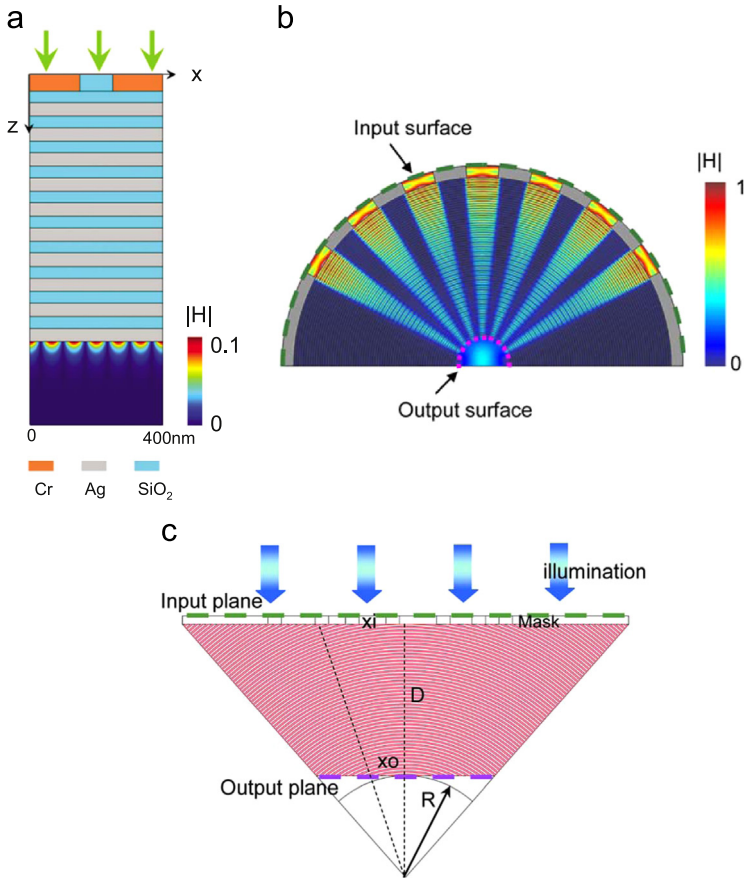

Fig. 18. (a) Nanolithography assisted by a ML slab: light (green arrows) incident on a 1D mask is converted into a sub-diffraction pattern. The color diagram represents the simulated magnitude of the H-field after the ML. Only one period (400 nm) of the Cr grating mask is shown. (b) Magnitude of the H-field in a cylindrical hyperlens used for nanolithography, showing the conversion of a 1D diffraction-limited pattern at the input surface into a sub-diffraction-limited one at the output surface. (c) Schematic of nanolithography with a flat interface hyperlens. (a) reproduced from Ref. [115], (b) and (c) from Ref. [116]. (For interpretation of the references to color in this figure caption, the reader is referred to the web version of this paper.)

3.2. Spontaneous emission engineering

Solid state lighting [117,118], optical communications [119], quantum computing with single photons [120,121] and fluorescence imaging [122] are examples of research fields where enhancing spontaneous emission from quantum sources (single atoms, ions or molecules, quantum dots, electron–hole pairs in quantum wells, color and nitrogen-vacancy centers in diamond, defects in SiC) is highly desirable. Such quantity depends not only on the dipole moment $\boldsymbol{\mu}$ of the transition, but also on the electromagnetic environment that hosts the emitter [12]. Fermi's golden rule states indeed that an initial excited state with 0 photons $|i, 0_{\mathbf{k}}\rangle$ decays

into a final state $|f, 1_{\mathbf{k}}\rangle$ with 1 photon of wavevector $\mathbf{k}$ at a rate [123]

$$\Gamma_{fi} = \frac{2\pi}{\hbar}\left|\langle f, 1_{\mathbf{k}}|H_{int}|i, 0_{\mathbf{k}}\rangle\right|^2 \rho(\hbar\omega_{\mathbf{k}}). \tag{23}$$

where $\hbar$ is Dirac's constant, $H_{int} = \boldsymbol{\mu} \cdot \mathbf{E}$ is the Hamiltonian of interaction between the dipole moment and the electric field $\mathbf{E}$ and ρ is the photonic density of states (PDOS), namely the density of available final photon states with frequency $\omega_{\mathbf{k}} = \omega_{fi}$, the transition frequency. ρ can be increased with respect to its value inside a homogeneous dielectric medium, conventionally termed "free space", by suitably designing the emitter's surroundings.

The concept of SE engineering was originally explored by Purcell, who quantified the ratio between the SE rate in a cavity at radio frequencies and the SE rate in free space as $F_P = (3\lambda_0^3 Q)/(4\pi^2 n^3 V)$ [124]. This *Purcell factor* relates the SE enhancement at the resonant wavelength $\lambda = \lambda_0/n$ to the quality factor Q and the mode volume V of a cavity with refractive index n. The Purcell factor has been extended as a figure of merit to optical cavities of micrometric [125] and nanometric sizes, for instance formed by defects in photonic crystals [119] or by metallic-coated semiconductor pillars [126]. The imperfect confinement of radiation at nanoscale requires Purcell enhancement to be deducted either indirectly from lifetime measurements [119] or by properly redefining Q and V [126].

Plasmonics offers to SE engineering a physical route alternative to the constructive interference exploited in cavities. An emitter embedded in a dielectric medium within the near-field of a metallic flat surface relaxes from an excited state via three competing processes: the emission of a photon that propagates in the far field, the emission of a surface plasmon polariton bound to the metal/dielectric interface, and the generation of lossy surface waves, that account for electron scattering and electron-hole excitation [127,128]. A SPP increases the PDOS by channeling the emission into k-vectors larger than those accessible with photons ($k > k_0$); nevertheless, it constitutes a decay route inherently radiative, although to be observed in the far field it requires a natural (metallic surface roughness) or artificial (dispersion of nano-sized scatterers on the metallic surface, periodic nanopatterning of said surface) outcoupling mechanism [117].

Both the cavity and the SPP approach have the intrinsic disadvantage of being resonant processes, which limits the overlap of the enhanced modes with the emission spectrum of the source. HMMs overcome these drawbacks thanks to their peculiar structure [129]. In a ML HMM, several parallel metal/dielectric interfaces are aligned at distances of a few tens of nanometers from each other. The mutual interaction of these interfaces, which individually support the same plasmonic resonance, results in a hybridized response [130,131]. In other words, the single plasmonic mode of a conventional metal/dielectric boundary (Fig. 19(a)) is replaced by multiple modes which cover a broader portion of the frequency spectrum (Fig. 19(b)). The same kind of coupling occurs between the metallic rods of a NW HMM, except in this case not only propagating surface plasmons but also localized surface plasmons are involved.

The SE enhancement allowed by HMMs possesses therefore the unique feature of being broadband. It is also easily tunable at the design stage by adjusting the metal filling ratio p [26]. The efficiency of such a mechanism is inevitably reduced by the ohmic losses associated with the metallic constituent [132]. Nonetheless, compared to a bulk metallic medium of the same size (corresponding to a filling ratio p of 1), a HMM displays lower ohmic dissipation, as the percentage of metal in the structure is always less than 100% ($p < 1$).

The capability of increasing the decay rate can be directly inferred from the anisotropic properties of hyperbolic media. A mode-counting procedure in k-space shows indeed that the

PDOS at the angular frequency ω is proportional to the shell delimited by the isofrequency surfaces at ω and $\omega + d\omega$ [37]. In the case of an isotropic environment, such shell is spherical: therefore, it encloses a limited portion of the k-space, resulting in a finite PDOS. In the frequency range where a material behaves ideally as hyperbolic, the shells become instead hyperboloidal, and as such unbounded, leading to a broadband singularity in the PDOS. In real implementations, the number of available photon states is prevented from becoming infinite by several factors [133,129]. First, the finite size a of the unit cell imposes an upper limit $k_{max} \sim 1/a$ to the maximum k-vector supported by the metamaterial along the direction of periodicity; accordingly, $\rho \sim k_{max}^3$ [37,129,133–135]. It was shown that the PDOS becomes infinite only in the limit of infinitesimally small emitter; a realistic spherical source of characteristic size s can achieve a maximum Purcell factor $\sim \lambda_0^3/s^3$ [135]. Furthermore, a finite distance from the HMM limits the access of the emitter to the largest k-vectors potentially available [129]. Finally, describing the permittivity of the metallic constituent of a ML with the hydrodynamic Drude model introduces spatial dispersion, which in turn leads to an upper bound to the PDOS proportional to ω^2/v_F^3, where v_F is the electron Fermi velocity of the metal [52].

As mentioned in the previous paragraph, to evaluate the SE enhancement induced by HMMs one can associate to such structures a suitable Purcell factor. Rather than adapting the original formula by Purcell, which is difficult since the radiation confinement is not as strong as in a cavity, a reasonable solution is to compute straightforwardly $F_P = \Gamma_{HMM}/\Gamma_0$, where Γ_{HMM} and Γ_0 are the SE rates in the presence of the hyperbolic environment and in free space.

This ratio can be obtained by means of the dyadic Green function $\overline{\overline{G}}$, a mathematical tool utilized to predict the emission patterns of point-like sources inside different environments [12]. In hyperbolic media, both the electric field of a point dipole and the associated Poynting vector exhibit a characteristic conical shape, due to the anisotropic wave propagation discussed in Section 2.1 [136,134]. The Green tensor was used to determine the Purcell factor of a single dipole embedded in a homogeneous hyperbolic space [136] and in an infinite cubic lattice of interacting dipoles in vacuum, where the hyperbolic properties were contained in the polarizability $\overline{\overline{\alpha}}$ of the individual grid elements (Discrete Dipole Approximation) [134]. In the case of layered media, $\overline{\overline{G}}$ in the half-space above the ML can be obtained by adding up the free space field and the field reflected from the

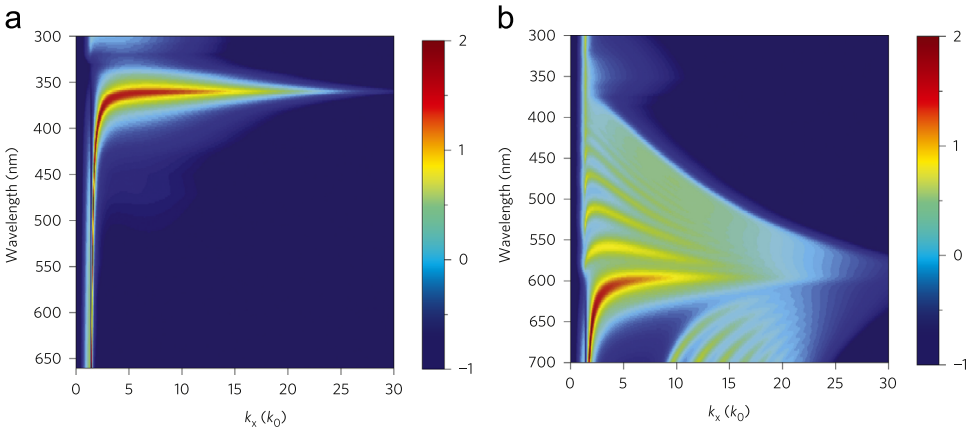

Fig. 19. Normalized dissipated power spectra (intensity on a logarithmic scale) for a dipole perpendicular to and at a distance of $d = 10$ nm above a uniform Ag single layer (a) and a Ag/Si multilayer HMM (b), each with the same total thickness of 305 nm. Reproduced from Ref. [26].

anisotropic region, retrieved with a transfer matrix method [40] or with an effective transmission line theory [137]. Effective permittivities accounting for a nonlocal metallic response were implemented in the Green function of a ML HMM, and were predicted to suppress the singularity of Purcell factors computed in local approximation [52].

An approach alternative to the one discussed above extends the tractation of Ford and Weber, who developed a SE enhancement formula for single plasmonic interfaces [127], to the case of ML HMMs [23,26]. This semiclassical method approximates ratios of rates with ratios of powers, and is equivalent to a fully quantum theory in the weak coupling limit [138,139]. In [26,131], a method was proposed to compute the Purcell factor of uniform or nanopatterned HMM structures with Finite Element Method (FEM) simulations. A derivation of the Purcell factor for a medium with elliptical and hyperbolic dispersion in the framework of quantum optics was carried out in [140].

Several experiments have been conducted to demonstrate SE modification in HMMs for a variety of quantum sources [23,26,37–39,69,141]. The temporal signature of Purcell enhancement is a decrease in the lifetime of the emitters when the latter are dispersed within the near field of the hyperbolic medium. Fig. 20(a) shows the decay curves of single molecules separated by a 21 nm transparent spacer from different substrates of identical thickness 305 nm, represented by a single layer of dielectric (Al_2O_3), a single layer of metal (Au), and a ML of 8 dielectric/metal periods [37]. The introduction of a spacer is necessary, since excessively short distances from the metallic or the HMM surface would make quenching in metal the dominant decay channel. While the metallic substrate exhibits a faster decay than the dielectric one, due in part to plasmons excitation and in part to quenching, the ML achieves an even better performance thanks to its large number of hyperbolic states available and to the lower ohmic losses. SE can be enhanced also in NW media [69]. In Fig. 20(b), deposition on an Al_2O_3 template filled with Ag nanowires causes the lifetime of a laser dye, measured to be 760 ps on top of the void template, to drop to 125 ps. The comparison with Au and Ag substrates, where quenching due to ohmic losses is expected to be higher than in the HMM, connects again the observed change to the excitation of high-k propagating waves rather than of lossy waves. CdSe/ZnS quantum dots (QDs) were utilized to probe the optical topological transition (cf. Fig. 6) in a Ag/TiO_2 ML with filling ratio 29% [23]. When the wavelength λ_0 crossed the critical point $\lambda_{0,c} = 621$ nm, the effective parameters of

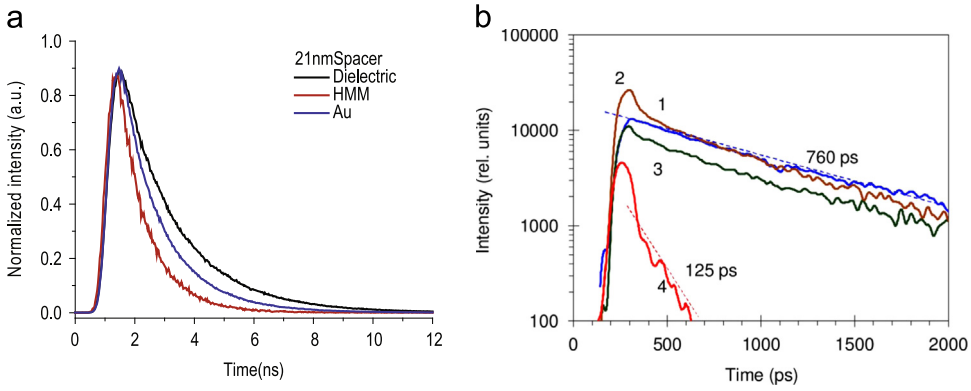

Fig. 20. Enhanced spontaneous emission of dye molecules on multilayer and nanowire HMMs. (a) SE dynamics of Rhodamine 800 excited at $\lambda_0 = 635$ nm on top of Al_2O_3 (black), Au (blue) and a Au/Al_2O_3 multilayer (red). (b) SE dynamics of IR140 excited at $\lambda_0 = 800$ nm on top of (1) a pure Al_2O_3 membrane, (2) a Au film on glass, (3) a Ag film on glass, and (4) a Ag/Al_2O_3 nanowire medium. (a) reproduced from Ref. [37], (b) from Ref. [69]. (For interpretation of the references to color in this figure caption, the reader is referred to the web version of this paper.)

said HMM evolved from the elliptic to the hyperbolic regime. The corresponding increase in the PDOS manifested itself in a shortening of lifetime, clearly discernible in Fig. 21. For the present application, the choice of QDs was critical: their photoluminescence (PL), peaked at $\lambda_{0,c}$, had a full-width at half-maximum (FWHM) of ~ 40 nm, which allowed the characterization of both the elliptical and the hyperbolic behavior on the same sample. Even larger FWHMs are exhibited by nitrogen-vacancy (NV) centers in diamond, promising candidates for the field of quantum information as they show single-photon generation and long spin coherence times [142]. An efficient production of quantum bits relies on a broadband SE enhancement mechanism, essential to match the spectrally wide emission of these light sources. The interaction between NV centers in nanodiamonds and a Au/Al_2O_3 ML was studied in a recent work [39]. Over the spectral interval 650–720 nm, the average lifetime on top of the HMM was reduced by a factor of 13.48 with respect to a control sample (Fig. 22), resulting in an experimental Purcell factor of 2.57. Finally, SE enhancement when the source is located inside a HMM rather than on top of it was explored experimentally, by functionalizing layers of dielectric with dye molecules [43], and with theoretical studies [131,138]. A dynamically tunable Purcell enhancement can be achieved at far-infrared frequencies if the metal layers are replaced with graphene sheets [28,30].

Despite the emission speed is increased in the presence of HMM substrates, the emission intensity is always concomitantly reduced. The high-wavevector states responsible for the SE enhancement are indeed propagating inside the hyperbolic medium, but become immediately evanescent as they enter the outer isotropic space. As a result, the net amount of radiation that reaches the far field is decreased with respect to free space, unless a conversion mechanism is introduced that outcouples the "trapped" waves. The extra k-vector that impedes propagation in free space can be lost by scattering with natural or artificial corrugations of the HMM surface, such as nanoparticles or gratings with various geometries and shapes (Fig. 23(a) and (b)) [26,131]. Fig. 23(c) and (d) shows the dependence of Purcell factor and intensity enhancement on the period of 1D gratings with rectangular profile patterned in a Ag/Si ML. As the grating period is decreased, both quantities increase, the change becoming more marked below 150 nm. A finer periodicity results indeed in a better match with high-k plasmonic modes; a period of

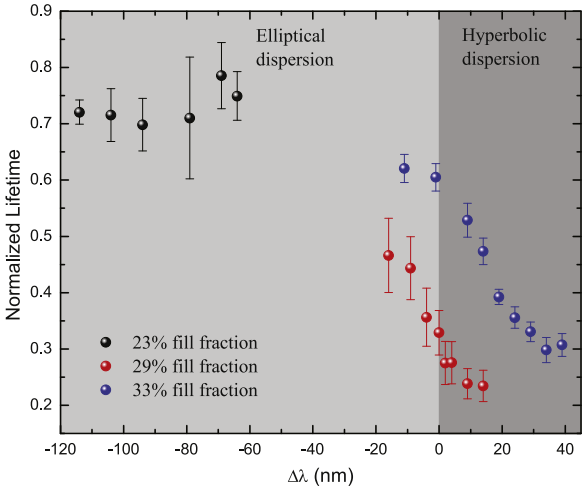

Fig. 21. Lifetime of CdSe/ZnS colloidal quantum dots on top of Ag/TiO_2 MLs with different filling ratios, normalized to the control samples. $\Delta\lambda$ represents the detuning with respect to the topological transition wavelength, $\lambda_{0,c} = 621$ nm, at the filling fraction 29%. Reproduced from Ref. [23].

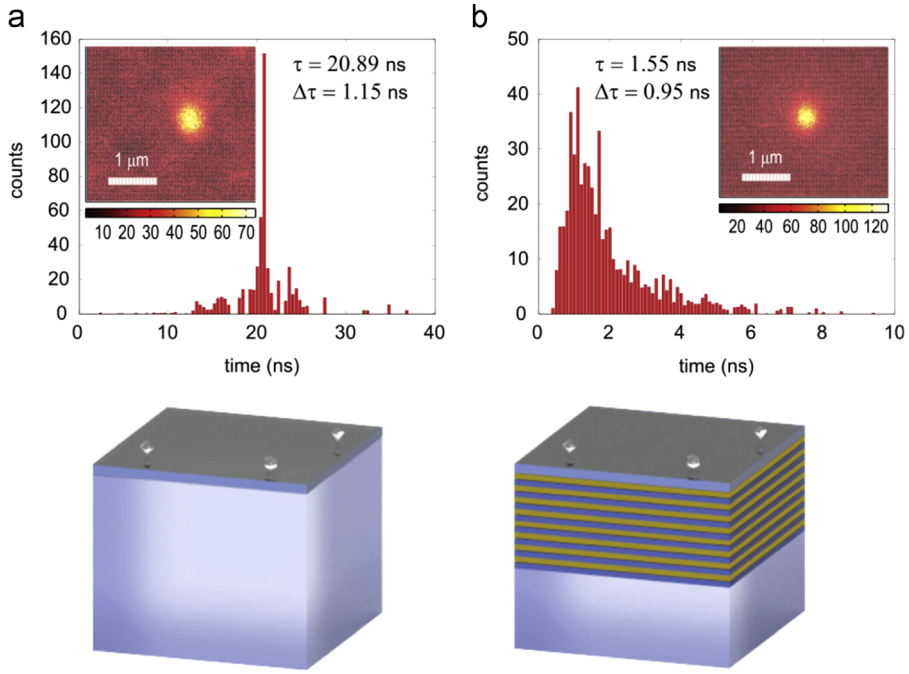

Fig. 22. Histograms of spontaneous emission lifetimes of Nitrogen-Vacancy centers in diamond on top of (a) a glass coverslip (control sample) and (b) an Al_2O_3 multilayer. The corresponding mean value and standard deviation of the lifetime distribution are (a) 20.89 ns and 1.15 ns, (b) 1.55 ns and 0.95 ns. Reproduced from Ref. [39].

80 nm reaches a Purcell factor as high as 76, and an intensity enhancement with respect to an unpatterned ML close to 80-fold, much higher than the 8-fold one achieved with larger periods.

3.3. Thermal emission engineering

The power emission of a black body at thermal equilibrium is ruled by Planck's law. Although this limit cannot be overcome in the far-field, the same is not true in the near-field, where the high PDOS of HMM leads to super-Planckian thermal emission [143]. The potential applications of this phenomenon span from energy harvesting and conversion to thermal coherent sources and thermal sinks [34,35]. In order to engineer heat transfer, researchers focussed their attention on SiC, a phonon-polaritonic metal where the real part of permittivity becomes negative in the infrared region inside the Reststrahlen band, delimited by the transverse and the longitudinal optical phonon resonance frequencies [34]. HMM MLs formed by stacks of SiC and SiO_2 layers exhibit three advantages. First, their high-k states can be thermally excited at moderate temperatures around 400–500 K, where the peak of the black body curve falls within the Reststrahlen band. Second, phonon-polaritonic metals have lower losses compared to plasmonic metals, and therefore the contribution of high-k modes dominates that of lossy surface waves. Third, as SiC/SiO_2 MLs operate in the wavelength interval 10–12 μm, the fabrication of subwavelength layers (period 50–100 nm) is relatively easy, and the effective medium theory is more accurate with respect to the optical range. For the same reason, the engineered near-field (distances $z \ll \lambda_0$) can be accessed experimentally with conventional detection systems.

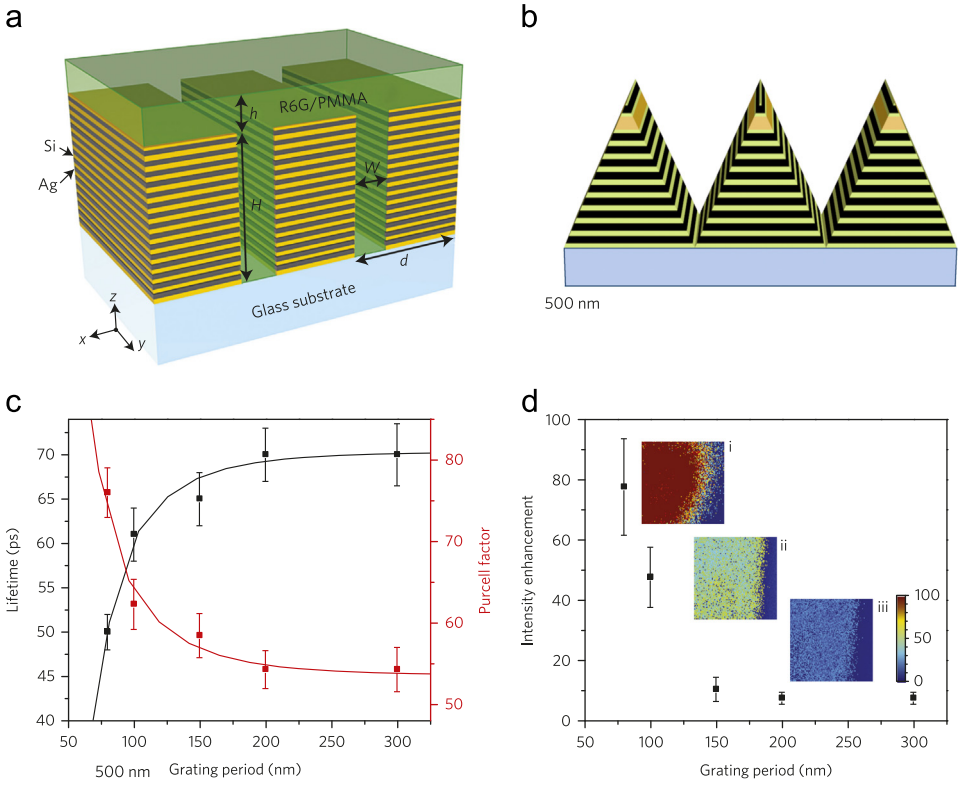

Fig. 23. (a) and (b) Outcoupling geometries for multilayer hyperbolic metamaterials. (a) Rectangular 1D grating patterned on a Ag/Si multilayer, with emitters contained in the green region. (b) Triangular 1D grating patterned on a Ag/Si multilayer, with emitters contained in the ochre region. (c) Spontaneous emission lifetime (black) and corresponding Purcell factor (red) for the dye molecule Rhodamine 6G on the nanopatterned Ag/Si multilayer of Fig. 23 (a), as a function of the grating period. The solid lines are a guide to the eye. (d) Fluorescence intensity enhancement for Rhodamine 6G on the nanopatterned Ag/Si multilayer of Fig. 23(a), as a function of the grating period. *Insets*: Optical images of the fluorescence intensity accumulated over 100 frames (grating periods: (i) $a=80$ nm; (ii) $a=100$ nm; (iii) $a=200$ nm). Error bars represent the fluctuations in fluorescence photo-counts. (a), (c) and (d) reproduced from Ref. [26], (b) from Ref. [131]. (For interpretation of the references to color in this figure caption, the reader is referred to the web version of this paper.)

The optical phase diagram of SiC/SiO_2 MLs is shown in Fig. 24(a). The emitted energy density of a HMM in equilibrium at temperature T, at distances z restricted to the near field and in the limit of low losses is given by [34]

$$u(z,\omega,T)^{z\ll\lambda_0} \approx \frac{U_{BB}(\omega,T)}{8}\left[\frac{2\sqrt{|\varepsilon_{xx}\varepsilon_{zz}|}}{(k_0 z)^3(1+|\varepsilon_{xx}\varepsilon_{zz}|)} - \varepsilon'' \frac{2(\varepsilon_{xx}+\varepsilon_{zz})}{(k_0 z)^3(1+|\varepsilon_{xx}\varepsilon_{zz}|)^2}\right], \tag{24}$$

where $U_{BB}(\omega,T)$ is the black body emission spectrum at temperature T, and ε_{xx}, ε_{zz} and ε'' are the real and imaginary parts of the permittivity components $\varepsilon_{\parallel}=\varepsilon_{xx}+i\varepsilon''$ and $\varepsilon_{\perp}=\varepsilon_{zz}+i\varepsilon''$ parallel and orthogonal to the layers. The first term represents the contribution of high-k modes, and greatly exceeds the second, related to lossy surface waves. Eq. (24) is plotted in Fig. 24(b) for a SiC/SiO_2 system; the comparison with the phase diagram of Fig. 24(a) highlights that emission enhancement is attained only in the hyperbolic regime, where the PDOS is larger.

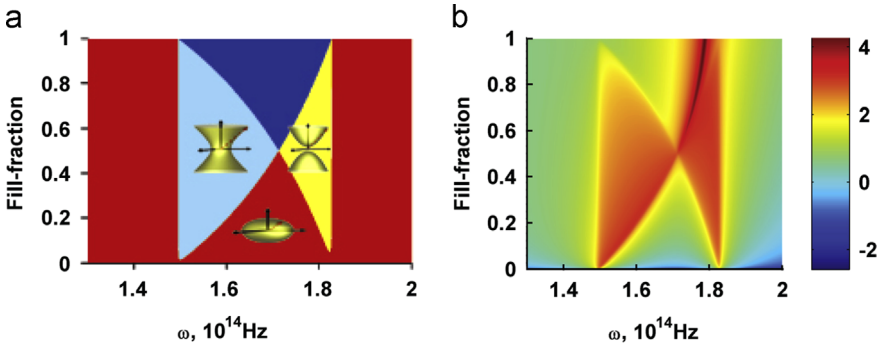

Fig. 24. (a) Optical phase diagram of a SiC/SiO_2 multilayer HMM showing the different optical isofrequency surfaces achieved in different regions. The dark blue area denotes an anisotropic effective metal where propagating waves are not allowed. (b) Super-Planckian thermal emission in the near field of the HMM (normalized to the black body radiation into the upper half-space) calculated analytically. Reproduced from Ref. [34]. (For interpretation of the references to color in this figure caption, the reader is referred to the web version of this paper.)

Thanks to their capability of altering near-field thermal emission, HMMs can increase heat transfer from and to materials which support infrared surface polariton resonances. A lattice of Au NWs in vacuum was shown to enhance non-resonantly the heat flux from a SiC emitter [144]. Heat exchange through a tiny gap between two SiC/SiO_2 ML HMMs exceeds the performance of analogously arranged black bodies, and is mainly influenced by the surface modes of the topmost layers [145].

Thermophotovoltaic devices require heat transfer at high temperatures and near-infrared frequencies; to this end, the operating range of thermal hyperbolic MLs can be tuned to 1–3 μm by utilizing aluminum zinc oxide (AZO, plasmonic metal) and TiO_2 [35].

3.4. Active and tunable devices

Like in many other metamaterials designed for exhibiting extraordinary optical properties, the performance of hyperbolic media is limited by the ohmic damping associated with free charge carriers, which imposes a cut-off on the achievable wavenumber of the propagating modes [141]. High wavenumbers correspond to a stronger concentration of electric field inside metals: as a consequence, the associated modes experience larger ohmic losses which prevent long propagation. This proves detrimental especially for the detection of sub-wavelength objects. It was shown numerically that lossless HMMs can achieve much higher resolution than those with realistic ohmic damping [94]. In addition, gain-compensated hypergrating structures were predicted to produce narrower focal points than their passive counterparts [146]. It is therefore desirable to incorporate gain materials, such as dye molecules and semiconductors, in the HMM design.

Thanks to the non-resonant nature of HMMs, loss compensation can be achieved with lower gain coefficients than those required by resonance-based artificial media. Numerical investigations were carried out to eliminate the influence of losses in metal/dielectric MLs [146–148]. TM-polarized propagating modes can be over-compensated by a gain medium with an imaginary part of the permittivity as low as $\varepsilon'' = -0.04$. This corresponds to a gain coefficient of about 2000 cm^{-1}. The above numerical studies only considered stimulated emission from the gain material. In addition, spontaneous emission can also be induced, which is undesirable for

imaging and focusing purposes as it produces blurring background. The noise generated by spontaneously emitted light is amplified, eventually reaching the so-called convective instability as the gain material gets pumped harder [147]. Therefore, the point of total compensation should be avoided for all the propagating modes in the HMM. To the best of our knowledge, a rigorous treatment incorporating the nonlinear dynamics of the carriers, such as exciton saturation, in the gain material has not been carried out, nor has the experimental demonstration of gain-assisted imaging or focusing been achieved.

Realistic candidates as gain media can be identified among the materials utilized in active plasmonics. Khurgin and Boltasseva [132] estimate that a gain of the order of 10^3–10^4 cm^{-1} is required to compensate for the ohmic damping in metals. This value is attainable in semiconductors with an injected carrier density of $\sim 10^{18}$ cm^{-3}, although the pumping current density needed to maintain such a concentration might be unpractical. Stimulated emission of SPPs has been observed in the visible and near infrared region in structures including, besides electrically pumped semiconductor gain media [126,149], a dye solution [150,151], a dye-doped polymer [152–155], dye-doped SiO_2 shells [156], Er-doped SiO_2 [157], a quantum-dot-doped polymer [158], and CdS nanowires [159]. A direct measurement of gain in propagating SPPs was reported by De Leon and Berini [151]. The analyzed structure consists in a symmetric Au-stripe waveguide, 20-nm thick and 1-μm wide, deposited on SiO_2 and covered with a gain layer of IR140 dye molecules in solution (1 mM concentration). When the latter are optically pumped, not only the losses are totally compensated, but the power of the probe beam coupled out of the structure is also 10% larger than the injected one. Several details govern the effectiveness and the repeatability of the active operation regime: (1) the gain anisotropy, determined by the relative polarization of the probe (cw Ti:sapphire laser) with respect to the pump (pulsed Nd:YAG laser); (2) the duration of the measurement, as the dye molecules – in the absence of recirculation of the solution – undergo photochemical modifications after 5 min of pump and probe illumination; (3) the thermal stability of the solution, that needs to be thermo-electrically cooled and enclosed in a dry environment to prevent thermo-optic modifications of its refractive index; (4) the local heating of the metal film during the pump pulse, resulting in a slight islandization of the film itself and therefore in a degraded performance; (5) the possible pulse-to-pulse energy variations of the pump signal, which can be taken into account by averaging the gain measurement over multiple pump pulses. Another experiment demonstrated an active negative-index metamaterial based on a fishnet structure [154]. The gain medium is represented here by a 50-nm epoxy layer doped with Rh800 dye (20 mM concentration), sandwiched between two 50-nm Ag layers. The material gain, extracted by matching numerical simulations with the experimental measurements, results in 2800 cm^{-1}. Salient aspects of the device characterization are: (1) the use of the same source (pulsed Ti:sapphire laser) to generate both the pump and the probe pulses; (2) the optimization of the time delay between the pump and the probe pulses, to ensure that the dye offers the maximum gain; (3) the use of an average pump power of 1 mW, below the damage threshold for the sample but 5 times larger than the gain saturation power of the doped epoxy; (4) photobleaching of the dye molecules, observed after 5 min of illumination; (5) the good match between optical measurements without pump and with a detuned delay between pump and probe (i.e. the pump is turned on, but does not operate effectively), which excludes influences from the setup or local heating.

A tunable behavior can be achieved in ML HMMs by means of graphene, a material that supports plasmonic resonances in the THz frequency range [108,160,161]. Its attractive features include low loss, high confinement of electromagnetic energy and fast response time. The conductivity of graphene can be tuned by shifting the Fermi level with an external electric field.

This suggests that a dramatic optical phase change from the elliptical to the hyperbolic regime through the ENZ point can be induced in graphene-based MLs by varying the electrical doping level [28,30,162]. The ultrathin graphene sheets, with their strong in-plane polarizability[3] [164], would play the role of the metal, with the further advantage of lower absorption and a reduced overall ML thickness.

The integration of graphene in ML hyperbolic structures was proposed and theoretically investigated in recent works [28,30,31]. A controllable elliptic–hyperbolic phase transition would imply sharp changes in reflection and transmission through the HMM, in the near-field absorption properties and in the Purcell effect.

3.5. Emerging topics

By virtue of the high k-vectors supported, ML HMMs can be shaped into deep sub-wavelength three-dimensional cavities (Fig. 25(a)), with sizes down to $\lambda/12$ [47,166]. In addition to the extreme confinement, HMM resonators also exhibit anomalous scaling properties: cavities of different sizes resonate at the same frequency, and higher-order modes oscillate at lower frequencies. The radiative quality factors Q_{rad} were shown to scale according to the universal power law $Q_{rad} \approx n_{eff}^4$, where $n_{eff} = k/k_0$ represents the effective refractive index of the resonator.

Rainbow trapping of electromagnetic fields in tapered HMM waveguides was discussed in [165,167]. Broadband light trapping can be realized by slowing down radiation in stop bands corresponding to different frequency-dependent positions along the waveguide [168–170]. In the proposed HMM approach, ML waveguides are tapered along the direction orthogonal to the layers, allowing normally incident waves to be directly coupled and stored inside the structures (Fig. 25(b)). The absorption spectrum of a Au/Ge device [165] shows a broadband response in the near-infrared range (Fig. 25(c)), with light of different wavelengths being concentrated in different layers (Fig. 25(d)). The operating range of HMM waveguide absorbers can be extended to mid-infrared frequencies with a proper material choice. In addition to rainbow trapping, other light absorption schemes that benefit from the large PDOS of HMMs were investigated theoretically and experimentally [44,137,171,172].

When two Ag/Ge ML hyperbolic waveguides are separated by a nanoscale air gap (Fig. 26(a)), an excitation beam directed along the slit causes the insurgence of giant optical forces up to 8 nN μm^{-1} mW^{-1} [173]. This phenomenon is induced by the large effective refractive indices $n_{eff,z} = k_z/k_0$ inside the two HMMs and their strong dependence on the slit size. The generated forces tend to attract the two HMM waveguides, and are transverse to the power flux of the beam. Thanks to the non-resonant nature of hyperbolic media, the described optical interaction can be triggered by a broadband excitation.

A dipole placed in a hyperbolic volume experiences a self-induced torque, originating from spatial anisotropy [174]. Spontaneously emitted photons exert reaction forces on the dipole that produces them. In an isotropic environment, two photons emitted into opposite directions generate forces that cancel each other. However, when the dipole is placed in an anisotropic medium and its orientation is misaligned with respect to the principal axis, its radiation pattern becomes asymmetric. As a consequence, a net restoring torque tends to align the dipole with the medium (Fig. 26(b)). The large PDOS enhances the emission rate, and therefore strengthens the phenomenon: the torque experienced by a dipole in a ML HMM is at least an order of magnitude higher than that in an anisotropic dielectric medium.

[3] As already mentioned, graphite, naturally consisting of stacked graphene layers, exhibits indefinite permittivity tensors both in the ultraviolet and in the THz region [20,163].

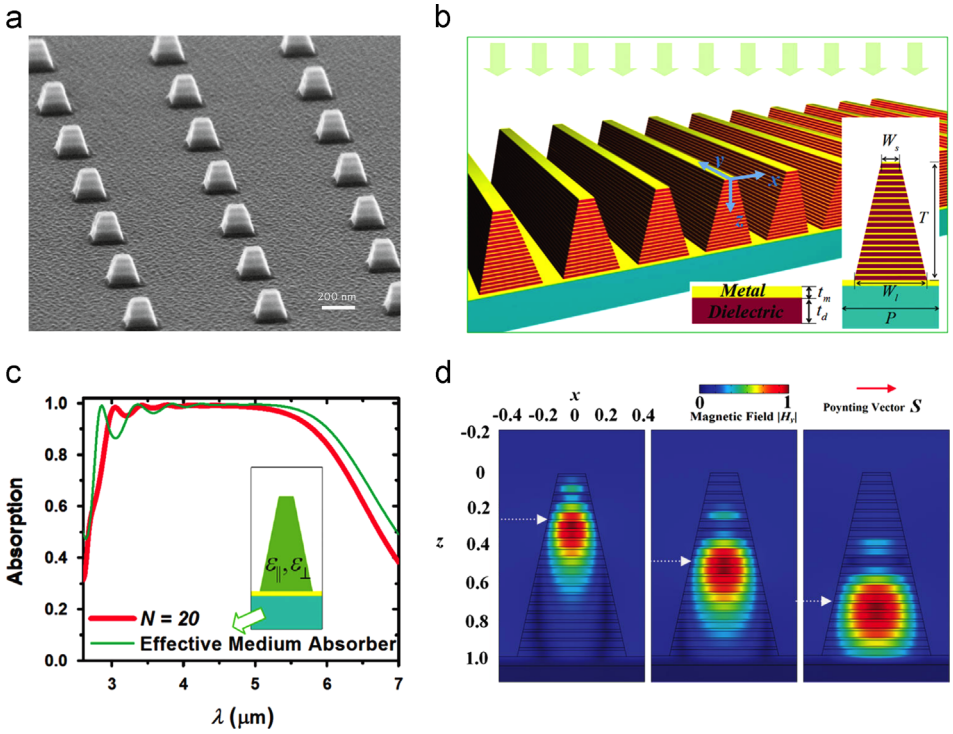

Fig. 25. (a) SEM image of an indefinite optical cavity array composed of Ag/Ge multilayers. (b) Schematic of a broadband absorber based on tapered HMM waveguides. (c) and (d) show respectively the absorption spectrum of the structure (N=number of periods) and the distribution of magnetic field at increasing wavelengths (left to right: λ_0=3.5 μm, λ_0=4.5 μm, λ_0=5.5 μm). (a) reproduced from Ref. [47], (b), (c) and (d) from Ref. [165].

The Casimir force in a lattice of metallic nanowires embedded in three dielectric fluids was studied in [175]. Such effect originates from the quantum zero-point energy, and plays a significant role in micromechanical systems [176]. The two interfaces at distance d formed by the fluids induce a restoring Casimir torque on the nanowires if the latter are misaligned with respect to the equilibrium position (normal to the interfaces); this interaction scales as $1/d$, in contrast to the $1/d^3$ law predicted for two parallel birefringent plates in vacuum [177].

4. Limitations of the effective medium description and quantum size effect

We have highlighted during our analysis of SE in HMM (Section 3.2) how, in addition to absorption, the finite period size, the internal structure of the emitter and the non-vanishing distance between the source and the HMM remove the PDOS divergence dictated by the EMT. The deviation from the effective medium description in finite-sized HMMs can be modeled as a nonlocal effect, so that the permittivity components become functions not only of the frequency, but also of the wavevector [49,133]. A comparison between local (hyperbolic medium with effective parameters) and nonlocal (real layered structure) dispersion is shown in Fig. 27(a)–(c). It was found that in finite-sized structures two propagating modes can occur simultaneously near the ENZ point [49,178]. Such coexistence of both forward and backward propagating waves is

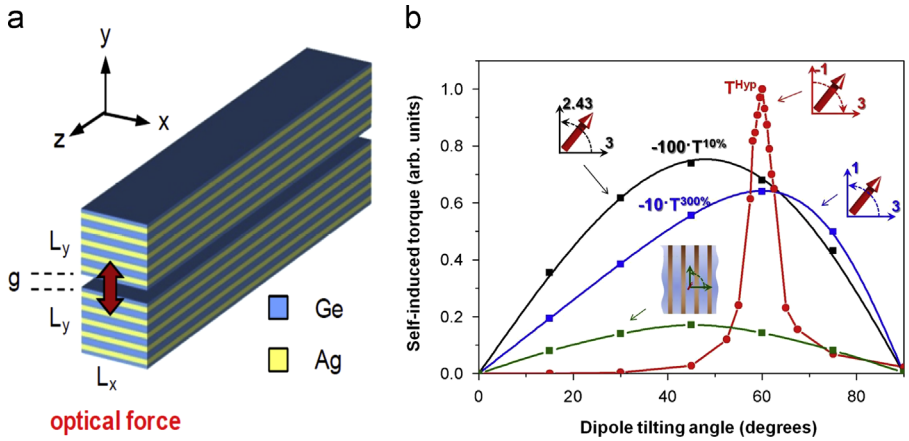

Fig. 26. (a) Transverse optical force (red arrows) induced on two HMM waveguides by a driving beam directed along the slit. (b) Torque on a 2 nm size dipole situated in media with different anisotropies as a function of its tilting angle with respect to the extraordinary axis: $\varepsilon_\perp = 2.42$, $\varepsilon_\parallel = 3$ (black squares), $\varepsilon_\perp = 1$, $\varepsilon_\parallel = 3$ (blue squares), $\varepsilon_\perp = -1$, $\varepsilon_\parallel = 3$ (red circles), layered metamaterial with effective parameters $\varepsilon_\perp = -1 - 0.2i$, $\varepsilon_\parallel = 2.9$, not scaled (green squares). Black and blue lines are analytical fits, red and green lines are guides for the eye. The rotation directions are indicated in the insets. (a) reproduced from Ref. [173], (b) from Ref. [174]. (For interpretation of the references to color in this figure caption, the reader is referred to the web version of this paper.)

not predicted by the EMT, and leads to an anomalous refraction behavior at the air-HMM interface (Fig. 27(d)–(f)).

When approaching the limit of extremely small unit cells (of the order of few nanometers and less), the effect of electronic confinement in the metal constituents (quantum size effect) needs to be considered. In a classical picture, where the charge carriers in metals move independently from each other, the electric displacement field D is described by means of a local response function:

$$D(\omega, \mathbf{r}) = \varepsilon(\omega, \mathbf{r})\varepsilon_0 E(\omega, \mathbf{r}), \tag{25}$$

where $\varepsilon(\omega, \mathbf{r})$ is the relative permittivity, ε_0 the vacuum permittivity, E the electric field, ω the angular frequency and $\mathbf{r}$ the position. As the metal size is progressively reduced, such approximation becomes inadequate, and a representation of light–matter interaction is required that includes the nonlocal response [179–182]. In this case, the displacement field is given by

$$D(\omega, \mathbf{r}) = \int \varepsilon(\omega, \mathbf{r}, \mathbf{r}')\varepsilon_0 E(\omega, \mathbf{r}')\, d\mathbf{r}', \tag{26}$$

namely it depends on the neighboring E-field distribution rather than only on the local field. The nonlocal response cannot be neglected when the characteristic dimensions (such as particle size, nanowire width, or gap size) approach the Coulomb screening length: at this point the electron–electron interaction needs to be taken into account.

We remark that this kind of nonlocal effect is different from the one discussed at the beginning of the subsection, which originated from the finite size of HMMs homogenized with the EMT. Yan et al. showed in [52], by implementing a hydrodynamic model for the permittivity of metal, that the PDOS of a ML HMM in a quantum nonlocal framework does not diverge as $1/a^3$ (a being the ML period). Instead, it reaches the maximum value $(c/v_F)^3$, where c is the speed of light and v_F is the Fermi velocity of the metal. The same model also implies that the hyperbolic

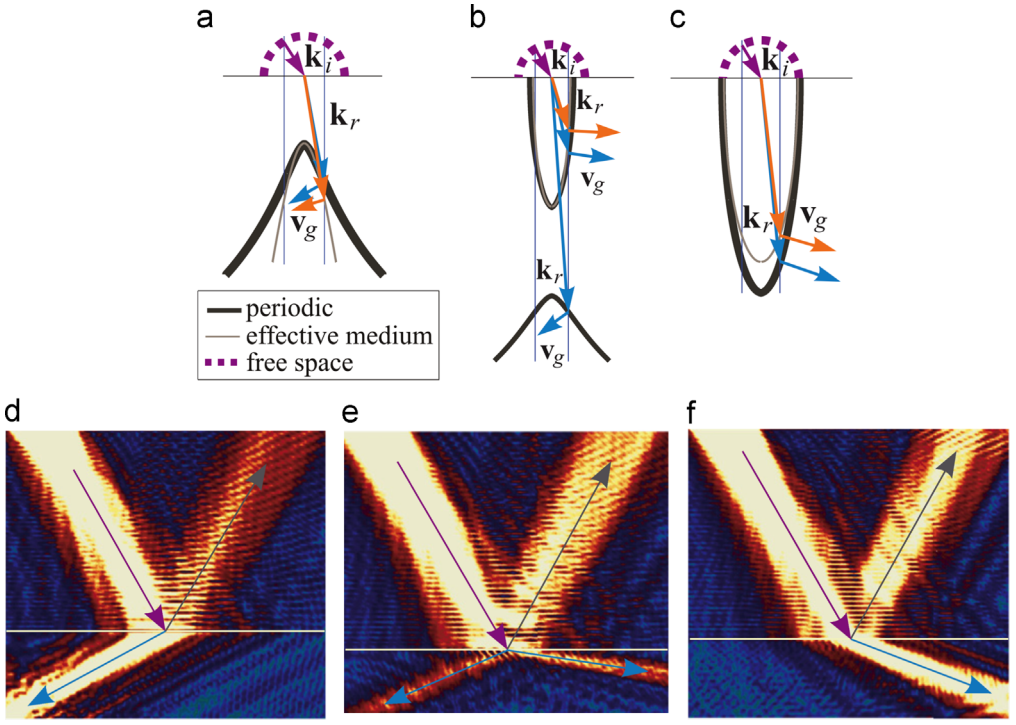

Fig. 27. Diagrams of beam refraction at the interface between air and a ML HMM with period D at three different frequencies: (a) $D/\lambda = 0.085$, (b) $D/\lambda = 0.094$, and (c) $D/\lambda = 0.106$. The wavevectors $\mathbf{k}_i$, $\mathbf{k}_r$ of the incident and refracted waves, respectively, and the group velocity $\mathbf{v}_g$ are plotted by means of the isofrequency contour method. The first Brillouin zone is rendered. (d–f) Numerical studies of the beam refraction in the three cases corresponding to figures (a–c). Reproduced from Ref. [49].

shape of the isofrequency contours is altered even if $a \ll \lambda_0$. The effects of nonlocal response on a hyperlens were analyzed in [54]. It was found that the optimal imaging frequency of the hyperlens is blueshifted with respect to analogous predictions based on the local response theory.

Ehsan et al. considered the propagation of quantum light states in a ML HMM with gain compensation [55]. They pointed out that the quantum noise or the quadrature variance of the E-field with a squeezed input state cannot be obtained using the conventional EMT, particularly in loss-compensated HMMs where it predicts vanishing quantum noise. Loss compensation in HMMs is not accompanied by quantum noise compensation, and quantum noise in ML HMMs is larger than in effective media. To formulate a quantum-optical EMT that successfully incorporated quantum noise in loss-compensated HMMs, Ehsan et al. introduced – besides effective permittivities – a new parameter, the effective noise distribution N_{eff}, that complements the description of photon propagation in HMMs.

5. Conclusions

The field of hyperbolic metamaterials originated from theoretical intuitions that found in plasmonics the key to be practically realized. A unique feature such as a tunable and

broadband response makes such media an exceptional tool of nanophotonics, and can speed up the transition from electronic to optical communications, both on a classical and on a quantum level.

Despite the increasing amount of theoretical works and proof-of-concept experiments, the leap towards the commercialization of the hyperbolic technology has been forbidden so far by a number of factors.

Absorption losses, inherently connected to the use of plasmonic metals at optical frequencies, represent a significant problem that can be mitigated by working at low filling ratios, implementing gain, or exploring alternative materials [183]. The PDOS mismatch between hyperbolic and free space makes it challenging to extract the information and the power carried by high-k states into the far field. Research in the incoming years should try to relax this bottleneck, by revisiting the geometry of hyperbolic structures or designing suitable outcoupling mechanisms (such as 1D or 2D gratings or nanoparticles with various sizes and shapes). A dynamic control of hyperbolic properties, extremely desirable in view of device production, has been proposed by means of graphene. Nonetheless, the extremely thin sheets of this material may be hard to integrate in a multilayer configuration, and the graphene-based technology is currently limited to the THz range. No alternatives capable of operating in the visible or the near-infrared range have emerged. Pushing the unit cells of MLs and NW arrays to sizes down to a few nanometers represents a further frontier that starts being approached. From the point of view of fundamental physics, the strong confinement of charge carriers and the scaling of material periodicity to the atomic level helps develop more accurate models of the radiation–matter interaction, including quantum effects, and can result in unprecedented phenomena. However, the experimental verification becomes challenging, as it is extremely sensitive to thermal and electrical sources of noise, and requires a clever setup design. Furthermore, the time-consuming and expensive manufacturing processes, together with the low degree of tolerance to defects of fabrication, can severely curtail the integration of quantum HMMs in out-of-lab applications.

In conclusion, hyperbolic media are currently a hot and evolving research topic. Aspects such as nonlinear and quantum effects still need to find a proper theoretical frame. The frequency control of thermal properties can lead to extremely efficient photovoltaic devices that optimize energy absorption and conversion. As scattering from HMMs can be strongly suppressed over large and tunable bands of frequency, these media may play a significant role for stealth technologies. Fluorescent tagging in the proximity of a hyperbolic environment can make faster and more efficient the detection of biomolecules. Finally, already proven concepts such as the hyperlens require further extensive studies, to conclusively assess – and overcome – their practical limitations. On the one side, given its thickness of hundreds of nm, a hyperlens can be integrated in an extremely thin smartphone or in a regular microscope, adding to them the capability of resolving the near field. On the other side, photolithography of nanoscale features by means of a hyperlens would represent a major breakthrough, as it would increase the density of data stored in optical devices, and of electrical components patterned on a chip.

Acknowledgments

The authors acknowledge financial support from the Office of Naval Research (ONR) Young Investigator Award (Grant no. N00014-13-1-0535), the Defense Advanced Research Projects Agency (DARPA) Young Faculty Award (Grant no. D13AP00054), the National Science

Foundation–Civil, Mechanical and Manufacturing Innovation (NSF-CMMI) (Grant no. 1120795). This project was partially supported by a Multidisciplinary University Research Initiative from the Air Force Office of Scientific Research (AFOSR MURI Award no. FA9550-12-1-0488).

References

[1] Y. Liu, X. Zhang, Chem. Soc. Rev. 40 (2011) 2494–2507.
[2] V.G. Veselago, Phys. Uspekhi 10 (1968) 509–514.
[3] V.M. Shalaev, Nat. Photon 1 (2007) 41–48.
[4] H. Raether, Surface Plasmons on Smooth and Rough Surfaces and on Gratings, Springer Tracts in Modern Physics, vol. 111, Springer, Berlin, Heidelberg, 1988.
[5] S. Maier, Plasmonics: Fundamentals and Applications: Fundamentals and Applications, Springer, New York, 2007.
[6] W.L. Barnes, A. Dereux, T.W. Ebbesen, Nature 424 (2003) 824–830.
[7] S.A. Maier, H.A. Atwater, J. Appl. Phys. 98 (2005) 011101.
[8] J.M. Pitarke, V.M. Silkin, E.V. Chulkov, P.M. Echenique, Reports Prog. Phys. 70 (2007) 1.
[9] C.L. Cortes, W. Newman, S. Molesky, Z. Jacob, J. Opt. 14 (2012) 063001.
[10] B. Wood, J.B. Pendry, D.P. Tsai, Phys. Rev. B 74 (2006) 115116.
[11] D.R. Smith, D. Schurig, Phys. Rev. Lett. 90 (2003) 077405.
[12] L. Novotny, B. Hecht, Principles of Nano-Optics, Principles of Nano-optics, Cambridge University Press, New York, 2012.
[13] S. Ishii, A.V. Kildishev, E. Narimanov, V.M. Shalaev, V.P. Drachev, Laser Photonics Rev. 7 (2013) 265–271.
[14] B. Saleh, M. Teich, Fundamentals of Photonics, Wiley Series in Pure and Applied Optics, Wiley, Hoboken, 2007.
[15] Y. Liu, G. Bartal, X. Zhang, Opt. Express 16 (2008) 15439–15448.
[16] J. Yao, Z. Liu, Y. Liu, Y. Wang, C. Sun, G. Bartal, A.M. Stacy, X. Zhang, Science 321 (2008) 930.
[17] C. Kittel, Introduction to Solid State Physics, 6th edition, John Wiley & Sons, Inc., New York, 1986.
[18] P. West, S. Ishii, G. Naik, N. Emani, V. Shalaev, A. Boltasseva, Laser Photonics Rev. 4 (2010) 795–808.
[19] L.V. Alekseyev, V.A. Podolskiy, E.E. Narimanov, Adv. OptoElectron. 2012 (2012).
[20] J. Sun, J. Zhou, B. Li, F. Kang, Appl. Phys. Lett. 98 (2011) 101901.
[21] R.K. Fisher, R.W. Gould, Phys. Rev. Lett. 22 (1969) 1093–1095.
[22] S. Rytov, Sov. Phys. JETP 2 (1956) 466–475.
[23] H.N.S. Krishnamoorthy, Z. Jacob, E. Narimanov, I. Kretzschmar, V.M. Menon, Science 336 (2012) 205–209.
[24] N. Engheta, Science 340 (2013) 286–287.
[25] A.J. Hoffman, L. Alekseyev, S.S. Howard, K.J. Franz, D. Wasserman, V.A. Podolskiy, E.E. Narimanov, D.L. Sivco, C. Gmachl, Nat. Mater. 6 (2007) 946–950.
[26] D. Lu, J.J. Kan, E.E. Fullerton, Z. Liu, Nat. Nano 9 (2014) 48–53.
[27] A. Boltasseva, H.A. Atwater, Science 331 (2011) 290–291.
[28] I.V. Iorsh, I.S. Mukhin, I.V. Shadrivov, P.A. Belov, Y.S. Kivshar, Phys. Rev. B 88 (2013) 039904.
[29] A.M. DaSilva, Y.-C. Chang, T. Norris, A.H. MacDonald, Phys. Rev. B 88 (2013) 195411.
[30] M.A.K. Othman, C. Guclu, F. Capolino, Opt. Express 21 (2013) 7614–7632.
[31] A. Andryieuski, A.V. Lavrinenko, D.N. Chigrin, Phys. Rev. B 86 (2012) 121108.
[32] T. Zhang, L. Chen, X. Li, Opt. Express 21 (2013) 20888–20899.
[33] D. Korobkin, B. Neuner III, C. Fietz, N. Jegenyes, G. Ferro, G. Shvets, Opt. Express 18 (2010) 22734–22746.
[34] Y. Guo, C.L. Cortes, S. Molesky, Z. Jacob, Appl. Phys. Lett. 101 (2012) 131106.
[35] Y. Guo, Z. Jacob, Opt. Express 21 (2013) 15014–15019.
[36] Z. Liu, H. Lee, Y. Xiong, C. Sun, X. Zhang, Science 315 (2007) 1686.
[37] Z. Jacob, J.-Y. Kim, G. Naik, A. Boltasseva, E. Narimanov, V. Shalaev, Appl. Phys. B 100 (2010) 215–218.
[38] J. Kim, V.P. Drachev, Z. Jacob, G.V. Naik, A. Boltasseva, E.E. Narimanov, V.M. Shalaev, Opt. Express 20 (2012) 8100–8116.
[39] M.Y. Shalaginov, S. Ishii, J. Liu, J. Liu, J. Irudayaraj, A. Lagutchev, A.V. Kildishev, V.M. Shalaev, Appl. Phys. Lett. 102 (2013) 173114.
[40] X. Ni, G. Naik, A. Kildishev, Y. Barnakov, A. Boltasseva, V. Shalaev, Appl. Phys. B 103 (2011) 553–558.

[41] K.V. Sreekanth, T. Biaglow, G. Strangi, J. Appl. Phys. 114 (2013) 134306.
[42] K.V. Sreekanth, A. De Luca, G. Strangi, Sci. Rep. 3 (2013).
[43] T. Tumkur, G. Zhu, P. Black, Y.A. Barnakov, C.E. Bonner, M.A. Noginov, Appl. Phys. Lett. 99 (2011) 151115.
[44] T.U. Tumkur, L. Gu, J.K. Kitur, E.E. Narimanov, M.A. Noginov, Appl. Phys. Lett. 100 (2012) 161103.
[45] J. Rho, Z. Ye, Y. Xiong, X. Yin, Z. Liu, H. Choi, G. Bartal, X. Zhang, Nat. Commun. 1 (2010) 143.
[46] G.V. Naik, J. Liu, A.V. Kildishev, V.M. Shalaev, A. Boltasseva, Proc. Natl. Acad. Sci. 109 (2012) 8834–8838.
[47] X. Yang, J. Yao, J. Rho, X. Yin, X. Zhang, Nat. Photonics 6 (2012) 450–454.
[48] L. Shen, T.-J. Yang, Y.-F. Chau, Phys. Rev. B 77 (2008) 205124.
[49] A.A. Orlov, P.M. Voroshilov, P.A. Belov, Y.S. Kivshar, Phys. Rev. B 84 (2011) 045424.
[50] A.V. Chebykin, A.A. Orlov, A.V. Vozianova, S.I. Maslovski, Y.S. Kivshar, P.A. Belov, Phys. Rev. B 84 (2011) 115438.
[51] A.V. Chebykin, A.A. Orlov, C.R. Simovski, Y.S. Kivshar, P.A. Belov, Phys. Rev. B 86 (2012) 115420.
[52] W. Yan, M. Wubs, N.A. Mortensen, Phys. Rev. B 86 (2012) 205429.
[53] S. Raza, T. Christensen, M. Wubs, S.I. Bozhevolnyi, N.A. Mortensen, Phys. Rev. B 88 (2013) 115401.
[54] W. Yan, N.A. Mortensen, M. Wubs, Opt. Express 21 (2013) 15026–15036.
[55] E. Amooghorban, N.A. Mortensen, M. Wubs, Phys. Rev. Lett. 110 (2013) 153602.
[56] P.A. Belov, R. Marqués, S.I. Maslovski, I.S. Nefedov, M. Silveirinha, C.R. Simovski, S.A. Tretyakov, Phys. Rev. B 67 (2003) 113103.
[57] M.G. Silveirinha, Phys. Rev. E 73 (2006) 046612.
[58] B.M. Wells, A.V. Zayats, V.A. Podolskiy, in: Conference on Lasers and Electro-Optics 2012, Optical Society of America, 2012, p. JTh2A.81.
[59] A.J. Kerman, E.A. Dauler, W.E. Keicher, J.K.W. Yang, K.K. Berggren, G. Gol'tsman, B. Voronov, Appl. Phys. Lett. 88 (2006) 111116.
[60] C.R. Simovski, P.A. Belov, A.V. Atrashchenko, Y.S. Kivshar, Adv. Mater. 24 (2012) 4229–4248.
[61] J. Yao, Y. Wang, K.-T. Tsai, Z. Liu, X. Yin, G. Bartal, A.M. Stacy, Y.-L. Wang, X. Zhang, Philos. Trans. R. Soc. A 369 (2011) 3434–3446.
[62] V.A. Podolskiy, E.E. Narimanov, Phys. Rev. B 71 (2005) 201101.
[63] J. Elser, R. Wangberg, V.A. Podolskiy, E.E. Narimanov, Appl. Phys. Lett. 89 (2006) 261102.
[64] G.D. Sulka, Highly Ordered Anodic Porous Alumina Formation by Self-Organized Anodizing, Wiley-VCH Verlag GmbH & Co. KGaA, Weinheim, 2008, pp. 1–116.
[65] P. Evans, W.R. Hendren, R. Atkinson, G.A. Wurtz, W. Dickson, A.V. Zayats, R.J. Pollard, Nanotechnology 17 (2006) 5746.
[66] M.A. Noginov, Y.A. Barnakov, G. Zhu, T. Tumkur, H. Li, E.E. Narimanov, Appl. Phys. Lett. 94 (2009) 151105.
[67] I.S. Nefedov, Phys. Rev. B 82 (2010) 155423.
[68] J. Yao, K.-T. Tsai, Y. Wang, Z. Liu, G. Bartal, Y.-L. Wang, X. Zhang, Opt. Express 17 (2009) 22380–22385.
[69] M.A. Noginov, H. Li, Y.A. Barnakov, D. Dryden, G. Nataraj, G. Zhu, C.E. Bonner, M. Mayy, Z. Jacob, E.E. Narimanov, Opt. Lett. 35 (2010) 1863–1865.
[70] A.V. Kabashin, P. Evans, S. Pastkovsky, W. Hendren, G.A. Wurtz, R. Atkinson, R. Pollard, V.A. Podolskiy, A.V. Zayats, Nat. Mater. 8 (2009) 867–871.
[71] I.I. Smolyaninov, HFSP J. 2 (2008) 129–131 PMID:19404465.
[72] E. Betzig, J.K. Trautman, Science 257 (1992) 189–195.
[73] S.W. Hell, Science 316 (2007) 1153–1158.
[74] B. Huang, W. Wang, M. Bates, X. Zhuang, Science 319 (2008) 810–813.
[75] N. Fang, H. Lee, C. Sun, X. Zhang, Science 308 (2005) 534–537.
[76] Z. Liu, S. Durant, H. Lee, Y. Pikus, N. Fang, Y. Xiong, C. Sun, X. Zhang, Nano Lett. 7 (2007) 403–408.
[77] X. Zhang, Z. Liu, Nat. Mater. 7 (2008) 435–441.
[78] S.A. Ramakrishna, J.B. Pendry, M.C.K. Wiltshire, W.J. Stewart, J. Mod. Opt. 50 (2003) 1419–1430.
[79] D.R. Smith, P. Kolinko, D. Schurig, J. Opt. Soc. Am. B 21 (2004) 1032–1043.
[80] P.A. Belov, Microw. Opt. Technol. Lett. 37 (2003) 259–263.
[81] T.G. Mackay, A. Lakhtakia, R.A. Depine, Microw. Opt. Technol. Lett. 48 (2006) 363–367.
[82] A. Fang, T. Koschny, C.M. Soukoulis, Phys. Rev. B 79 (2009) 245127.
[83] D.R. Smith, D. Schurig, J.J. Mock, P. Kolinko, P. Rye, Appl. Phys. Lett. 84 (2004) 2244–2246.
[84] H. Liu, Q. Lv, H. Luo, S. Wen, W. Shu, D. Fan, J. Opt. A: Pure Appl. Opt. 11 (2009) 105103.
[85] G. Li, J. Li, K.W. Cheah, Appl. Opt. 50 (2011) G27–G30.
[86] Z. Jacob, L.V. Alekseyev, E. Narimanov, Opt. Express 14 (2006) 8247–8256.
[87] D. Lu, Z. Liu, Nat. Commun. 3 (2012) 1205.

[88] H. Lee, Z. Liu, Y. Xiong, C. Sun, X. Zhang, Opt. Express 15 (2007) 15886–15891.
[89] E.J. Smith, Z. Liu, Y.F. Mei, O.G. Schmidt, Appl. Phys. Lett. 95 (2009) 083104.
[90] S. Han, Y. Xiong, D. Genov, Z. Liu, G. Bartal, X. Zhang, Nano Lett. 8 (2008) 4243–4247.
[91] A.V. Kildishev, V.M. Shalaev, Opt. Lett. 33 (2008) 43–45.
[92] B.H. Cheng, Y.Z. Ho, Y.-C. Lan, D.P. Tsai, IEEE J. Sel. Top. Quantum Electron. 19 (2013) 4601305.
[93] J.B. Pendry, S.A. Ramakrishna, J. Phys.: Condens. Matter 14 (2002) 8463.
[94] A. Salandrino, N. Engheta, Phys. Rev. B 74 (2006) 075103.
[95] V.M. Shalaev, Science 322 (2008) 384–386.
[96] W. Wang, H. Xing, L. Fang, Y. Liu, J. Ma, L. Lin, C. Wang, X. Luo, Opt. Express 16 (2008) 21142–21148.
[97] A.V. Kildishev, E.E. Narimanov, Opt. Lett. 32 (2007) 3432–3434.
[98] C. Ma, Z. Liu, Opt. Express 18 (2010) 4838–4844.
[99] C. Ma, Z. Liu, in: Imaging and Applied Optics Congress, Optical Society of America, 2010, p. MWB5.
[100] C. Ma, Z. Liu, Opt. Express 20 (2012) 2581–2586.
[101] A.V. Kildishev, U.K. Chettiar, Z. Jacob, V.M. Shalaev, E.E. Narimanov, Appl. Phys. Lett. 94 (2009) 071102.
[102] N. Gibbons, J.J. Baumberg, C.L. Bower, M. Kolle, U. Steiner, Adv. Mater. 21 (2009) 3933–3936.
[103] J. Kerbst, S. Schwaiger, A. Rottler, A. Koitmäe, M. Bröll, J. Ehlermann, A. Stemmann, C. Heyn, D. Heitmann, S. Mendach, Appl. Phys. Lett. 99 (2011) 191905.
[104] S. Schwaiger, M. Bröll, A. Krohn, A. Stemmann, C. Heyn, Y. Stark, D. Stickler, D. Heitmann, S. Mendach, Phys. Rev. Lett. 102 (2009) 163903.
[105] S. Schwaiger, A. Rottler, S. Mendach, Adv. OptoElectron. 2012 (2012) 10.
[106] D. Aronovich, G. Bartal, Opt. Lett. 38 (2013) 413–415.
[107] J. Wang, Y. Xu, H. Chen, B. Zhang, J. Mater. Chem. 22 (2012) 15863–15868.
[108] L. Ju, B. Geng, J. Horng, C. Girit, M. Martin, Z. Hao, H.A. Bechtel, X. Liang, A. Zettl, Y.R. Shen, F. Wang, Nat. Nano 6 (2011) 630–634.
[109] P.A. Belov, C.R. Simovski, P. Ikonen, Phys. Rev. B 71 (2005) 193105.
[110] G. Shvets, S. Trendafilov, J.B. Pendry, A. Sarychev, Phys. Rev. Lett. 99 (2007) 053903.
[111] A. Ono, J.-I. Kato, S. Kawata, Phys. Rev. Lett. 95 (2005) 267407.
[112] P. Ikonen, C. Simovski, S. Tretyakov, P. Belov, Y. Hao, Appl. Phys. Lett. 91 (2007) 104102.
[113] Y. Zhao, G. Palikaras, P.A. Belov, R.F. Dubrovka, C.R. Simovski, Y. Hao, C.G. Parini, New J. Phys. 12 (2010) 103045.
[114] B.D.F. Casse, W.T. Lu, Y.J. Huang, E. Gultepe, L. Menon, S. Sridhar, Appl. Phys. Lett. 96 (2010) 023114.
[115] Y. Xiong, Z. Liu, X. Zhang, Appl. Phys. Lett. 93 (2008) 111116.
[116] Y. Xiong, Z. Liu, X. Zhang, Appl. Phys. Lett. 94 (2009) 203108.
[117] K. Okamoto, I. Niki, A. Shvartser, Y. Narukawa, T. Mukai, A. Scherer, Nat. Mater. 3 (2004) 601–605.
[118] M. Francardi, L. Balet, A. Gerardino, N. Chauvin, D. Bitauld, L.H. Li, B. Alloing, A. Fiore, Appl. Phys. Lett. 93 (2008) 143102.
[119] G. Shambat, B. Ellis, A. Majumdar, J. Petykiewicz, M.A. Mayer, T. Sarmiento, J. Harris, E.E. Haller, J. Vučković, Nat. Commun. 2 (2011) 539.
[120] M.D. Eisaman, J. Fan, A. Migdall, S.V. Polyakov, Rev. Sci. Instrum. 82 (2011) 071101.
[121] J.H. Prechtel, A.V. Kuhlmann, J. Houel, L. Greuter, A. Ludwig, D. Reuter, A.D. Wieck, R.J. Warburton, Phys. Rev. X 3 (2013) 041006.
[122] H.G. Frey, S. Witt, K. Felderer, R. Guckenberger, Phys. Rev. Lett. 93 (2004) 200801.
[123] J. Dowling, Found. Phys. 23 (1993) 895–905.
[124] E.M. Purcell, Phys. Rev. 69 (1946) 681–681.
[125] K.J. Vahala, Nature 424 (2003) 839–846.
[126] M.T. Hill, Y.-S. Oei, B. Smalbrugge, Y. Zhu, T. de Vries, P.J. van Veldhoven, F.W.M. van Otten, T.J. Eijkemans, J.P. Turkiewicz, H. de Waardt, E.J. Geluk, S.-H. Kwon, Y.-H. Lee, R. Notzel, M.K. Smit, Nat. Photonics 1 (2007) 589–594.
[127] G. Ford, W. Weber, Phys. Rep. 113 (1984) 195–287.
[128] W.L. Barnes, J. Mod. Opt. 45 (1998) 661–699.
[129] O. Kidwai, S.V. Zhukovsky, J.E. Sipe, Phys. Rev. A 85 (2012) 053842.
[130] S.V. Zhukovsky, O. Kidwai, J.E. Sipe, Opt. Express 21 (2013) 14982–14987.
[131] L. Ferrari, D. Lu, D. Lepage, Z. Liu, Opt. Express 22 (2014) 4301–4306.
[132] J.B. Khurgin, A. Boltasseva, MRS Bull. 37 (2012) 768–779.
[133] O. Kidwai, S.V. Zhukovsky, J.E. Sipe, Opt. Lett. 36 (2011) 2530–2532.
[134] A.N. Poddubny, P.A. Belov, P. Ginzburg, A.V. Zayats, Y.S. Kivshar, Phys. Rev. B 86 (2012) 035148.

[135] A.N. Poddubny, P.A. Belov, Y.S. Kivshar, Phys. Rev. A 84 (2011) 023807.
[136] A.S. Potemkin, A.N. Poddubny, P.A. Belov, Y.S. Kivshar, Phys. Rev. A 86 (2012) 023848.
[137] C. Guclu, S. Campione, F. Capolino, Phys. Rev. B 86 (2012) 205130.
[138] W.D. Newman, C.L. Cortes, Z. Jacob, J. Opt. Soc. Am. B 30 (2013) 766–775.
[139] T. Hümmer, F.J. García-Vidal, L. Martín-Moreno, D. Zueco, Phys. Rev. B 87 (2013) 115419.
[140] Z. Liu, W. Li, X. Jiang, J.C. Cao, Phys. Rev. A 87 (2013) 053836.
[141] Z. Jacob, I.I. Smolyaninov, E.E. Narimanov, Appl. Phys. Lett. 100 (2012) 181105.
[142] Z. Jacob, V.M. Shalaev, Science 334 (2011) 463–464.
[143] S.-A. Biehs, M. Tschikin, P. Ben-Abdallah, Phys. Rev. Lett. 109 (2012) 104301.
[144] B. Liu, S. Shen, Phys. Rev. B 87 (2013) 115403.
[145] S.-A. Biehs, M. Tschikin, R. Messina, P. Ben-Abdallah, Appl. Phys. Lett. 102 (2013) 131106.
[146] X. Ni, S. Ishii, M.D. Thoreson, V.M. Shalaev, S. Han, S. Lee, A.V. Kildishev, Opt. Express 19 (2011) 25242–25254.
[147] R.S. Savelev, I.V. Shadrivov, P.A. Belov, N.N. Rosanov, S.V. Fedorov, A.A. Sukhorukov, Y.S. Kivshar, Phys. Rev. B 87 (2013) 115139.
[148] C. Argyropoulos, N.M. Estakhri, F. Monticone, A. Alù, Opt. Express 21 (2013) 15037–15047.
[149] M.T. Hill, M. Marell, E.S.P. Leong, B. Smalbrugge, Y. Zhu, M. Sun, P.J. van Veldhoven, E.J. Geluk, F. Karouta, Y.-S. Oei, R. Nötzel, C.-Z. Ning, M.K. Smit, Opt. Express 17 (2009) 11107–11112.
[150] J. Seidel, S. Grafström, L. Eng, Phys. Rev. Lett. 94 (2005) 177401.
[151] I. De Leon, P. Berini, Nat. Photonics 4 (2010) 382–387.
[152] M.A. Noginov, V.A. Podolskiy, G. Zhu, M. Mayy, M. Bahoura, J.A. Adegoke, B.A. Ritzo, K. Reynolds, Opt. Express 16 (2008) 1385–1392.
[153] M.A. Noginov, G. Zhu, M. Mayy, B.A. Ritzo, N. Noginova, V.A. Podolskiy, Phys. Rev. Lett. 101 (2008) 226806.
[154] S. Xiao, V.P. Drachev, A.V. Kildishev, X. Ni, U.K. Chettiar, H.-K. Yuan, V.M. Shalaev, Nature 466 (2010) 735–738.
[155] X. Meng, A.V. Kildishev, K. Fujita, K. Tanaka, V.M. Shalaev, Nano Lett. 13 (2013) 4106–4112.
[156] M.A. Noginov, G. Zhu, A.M. Belgrave, R. Bakker, V.M. Shalaev, E.E. Narimanov, S. Stout, E. Herz, T. Suteewong, U. Wiesner, Nature 460 (2009) 1110–1112.
[157] M. Ambati, S.H. Nam, E. Ulin-Avila, D.A. Genov, G. Bartal, X. Zhang, Nano Lett. 8 (2008) 3998–4001.
[158] J. Grandidier, G.C. des Francs, S. Massenot, A. Bouhelier, L. Markey, J.-C. Weeber, C. Finot, A. Dereux, Nano Lett. 9 (2009) 2935–2939.
[159] R.F. Oulton, V.J. Sorger, T. Zentgraf, R.-M. Ma, C. Gladden, L. Dai, G. Bartal, X. Zhang, Nature 461 (2009) 629–632.
[160] F.H.L. Koppens, D.E. Chang, F.J. García de Abajo, Nano Lett. 11 (2011) 3370–3377.
[161] V.W. Brar, M.S. Jang, M. Sherrott, J.J. Lopez, H.A. Atwater, Nano Lett. 13 (2013) 2541–2547.
[162] M.A.K. Othman, C. Guclu, F. Capolino, J. Nanophotonics 7 (2013) 073089.
[163] E. Palik, Handbook of Optical Constants of Solids, Academic Press Handbook Series, vol. 2, Academic Press, San Diego, 1991.
[164] S.H. Mousavi, I. Kholmanov, K.B. Alici, D. Purtseladze, N. Arju, K. Tatar, D.Y. Fozdar, J.W. Suk, Y. Hao, A.B. Khanikaev, R.S. Ruoff, G. Shvets, Nano Lett. 13 (2013) 1111–1117.
[165] Y. Cui, K.H. Fung, J. Xu, H. Ma, Y. Jin, S. He, N.X. Fang, Nano Lett. 12 (2012) 1443–1447.
[166] J. Yao, X. Yang, X. Yin, G. Bartal, X. Zhang, Proc. Natl. Acad. Sci 108 (2011) 11327–11331.
[167] H. Hu, D. Ji, X. Zeng, K. Liu, Q. Gan, Sci. Rep. 3 (2013).
[168] K.L. Tsakmakidis, A.D. Boardman, O. Hess, Nature 450 (2007) 397–401.
[169] J. Park, K.-Y. Kim, I.-M. Lee, H. Na, S.-Y. Lee, B. Lee, Opt. Express 18 (2010) 598–623.
[170] M.S. Jang, H. Atwater, Phys. Rev. Lett. 107 (2011) 207401.
[171] I.S. Nefedov, C.A. Valagiannopoulos, S.M. Hashemi, E.I. Nefedov, Sci. Rep. 3 (2013).
[172] E.E. Narimanov, H. Li, Y.A. Barnakov, T.U. Tumkur, M.A. Noginov, Opt. Express 21 (2013) 14956–14961.
[173] Y. He, S. He, J. Gao, X. Yang, Opt. Express 20 (2012) 22372–22382.
[174] P. Ginzburg, A.V. Krasavin, A.N. Poddubny, P.A. Belov, Y.S. Kivshar, A.V. Zayats, Phys. Rev. Lett. 111 (2013) 036804.
[175] T.A. Morgado, S.I. Maslovski, M.G. Silveirinha, Opt. Express 21 (2013) 14943–14955.
[176] F. Capasso, J. Munday, D. Iannuzzi, H.B. Chan, IEEE J. Sel. Top. Quantum Electron. 13 (2007) 400–414.
[177] J.N. Munday, D. Iannuzzi, Y. Barash, F. Capasso, Phys. Rev. A 71 (2005) 042102.
[178] S. Savoia, G. Castaldi, V. Galdi, Phys. Rev. B 87 (2013) 235116.
[179] J.M. McMahon, S.K. Gray, G.C. Schatz, Phys. Rev. Lett. 103 (2009) 097403.

[180] A.I. Fernández-Domínguez, A. Wiener, F.J. García-Vidal, S.A. Maier, J.B. Pendry, Phys. Rev. Lett. 108 (2012) 106802.
[181] A. Wiener, A.I. Fernández-Domínguez, A.P. Horsfield, J.B. Pendry, S.A. Maier, Nano Lett. 12 (2012) 3308–3314.
[182] T.V. Teperik, P. Nordlander, J. Aizpurua, A.G. Borisov, Opt. Express 21 (2013) 27306–27325.
[183] G.V. Naik, V.M. Shalaev, A. Boltasseva, Adv. Mater. 25 (2013) 3264–3294.